Null-Field Approach for the Multi-inclusion Problem Under Antiplane Shears

Jeng-Tzong Chen
e-mail: jtchen@mail.ntou.edu.tw

An-Chien Wu

Department of Harbor and River Engineering,
National Taiwan Ocean University,
Keelung 20224,
Taiwan

*In this paper, we derive the null-field integral equation for an infinite medium containing circular holes and/or inclusions with arbitrary radii and positions under the remote antiplane shear. To fully capture the circular geometries, separable expressions of fundamental solutions in the polar coordinate for field and source points and Fourier series for boundary densities are adopted to ensure the exponential convergence. By moving the null-field point to the boundary, singular and hypersingular integrals are transformed to series sums after introducing the concept of degenerate kernels. Not only the singularity but also the sense of principle values are novelly avoided. For the calculation of boundary stress, the Hadamard principal value for hypersingularity is not required and can be easily calculated by using series sums. Besides, the boundary-layer effect is eliminated owing to the introduction of degenerate kernels. The solution is formulated in a manner of semi-analytical form since error purely attributes to the truncation of Fourier series. The method is basically a numerical method, and because of its semi-analytical nature, it possesses certain advantages over the conventional boundary element method. The exact solution for a single inclusion is derived using the present formulation and matches well with the Honein et al.'s solution by using the complex-variable formulation (Honein, E., Honein, T., and Hermann, G., 1992, Appl. Math., **50**, pp. 479–499). Several problems of two holes, two inclusions, one cavity surrounded by two inclusions and three inclusions are revisited to demonstrate the validity of our method. The convergence test and boundary-layer effect are also addressed. The proposed formulation can be generalized to multiple circular inclusions and cavities in a straightforward way without any difficulty.* [DOI: 10.1115/1.2338056]

1 Introduction

The distribution of stress in an infinite medium containing circular holes and/or inclusions under the antiplane shear has been studied by many investigators. However, analytical solutions are rather limited except for simple cases. To the authors' best knowledge, an exact solution of a single inclusion was derived by Honein et al. [1] using the complex potential. Besides, analytical solutions for two identical holes and inclusions were obtained by Stief [2] and by Budiansky and Carrier [3], respectively. Zimmerman [4] employed the Schwartz alternative method for plane problems with two holes or inclusions to obtain a closed-form approximate solution. In addition, Sendeckyj [5] proposed an iterative scheme for solving problems of multiple inclusions. However, the approach is rather complicated and explicit solutions were not provided. Numerical solutions for problems with two unequal holes and/or inclusions were provided by Honein et al. [1] using the Möbius transformations involving the complex potential. Not only antiplane shears but also screw dislocations were considered. Numerical results were presented by Goree and Wilson [6] for an infinite medium containing two inclusions under the remote shear. Bird and Steele [7] used a Fourier series procedure to revisit the antiplane elasticity problems of Honein et al.'s paper [1]. To approximate the Honein et al.'s infinite problem, an equivalent bounded-domain approach with the stress applied on the outer boundary was utilized. A shear stress σ_{zr} on the outer boundary is used in place of a stress σ_{zy} at infinity to approach the Honein et al.'s results as the radius becomes large. Wu [8] solved the analytical solution for two inclusions under the remote shear in two directions by using the conformal mapping and the theorem of analytic continuation. Based on the technique of analytical continuity and the method of successive approximation, Chao and Young [9] studied the stress concentration on a hole surrounded by two inclusions. For a triangle pattern of three inclusions, Gong [10] employed the complex potential and Laurent series expansion to calculate the stress concentration. Complex variable boundary element method was utilized to deal with the problem of two circular holes by Chou [11] and Ang and Kang [12], independently. To provide a general solution to the antiplane interaction among multiple circular inclusions with arbitrary radii, shear moduli, and location is not trivial. Mathematically speaking, only circular boundaries in an infinite domain are concerned here. Mogilevskaya and Crouch [13] have also employed Fourier series expansion technique and used the Galerkin method instead of collocation technique to solve the problem of circular inclusions in 2D elasticity. The advantage of their method is that one can tackle a lot of inclusions even inclusions touching one another. However, they did not expand a fundamental solution into a degenerate kernel in the polar coordinate. Degenerate kernels play an important role not only for mathematical analysis [14] but also for numerical implementation. For example, the spurious eigenvalue [15], fictitious frequency [16], and degenerate scale [17] have been mathematically and numerically studied by using degenerate kernels for problems with circular boundaries. One gain is that exponential convergence instead of algebraic convergence in the boundary element method (BEM) can be achieved using the Fourier expansion [14]. Chen et al. [18] have successfully solved the antiplane problem with circular holes using the null-field integral equation in conjunction with the degenerate kernel and Fourier series. The

Contributed by the Applied Mechanics Division of ASME for publication in the Journal of Applied Mechanics. Manuscript received November 15, 2005; final manuscript received May 22, 2006. Review conducted by Z. Suo. Discussion on the paper should be addressed to the Editor, Prof. Robert M. McMeeking, Journal of Applied Mechanics, Department of Mechanical and Environmental Engineering, University of California–Santa Barbara, Santa Barbara, CA 93106-5070, and will be accepted until four months after final publication in the paper itself in the ASME Journal of Applied Mechanics.

PROOF COPY [JAM-05-1418] 008606AMJ

extension to biharmonic problems was also implemented [19]. This paper extends the idea to solve problems with circular inclusions.

By introducing a multidomain approach, an inclusion problem can be decomposed into two parts. One is the infinite medium with circular holes and the other is the problem with each circular inclusion. After considering the continuity and equilibrium conditions on the interface between the matrix and inclusion, a linear algebraic system is obtained and the unknown Fourier coefficients in the algebraic system can be determined. Then, the field potential and stress are easily obtained. Furthermore, an arbitrary number of circular inclusions can be treated by using the present method without any difficulty. One must take care the vector decomposition in using the adaptive observer system for the nonconfocal case. Also, the boundary stress is easily determined by using series sums instead of employing the sense of Hadamard principal value. A general purpose program for arbitrary number of circular inclusions with various radii and arbitrary positions was developed. The infinite medium with multiple circular holes [18] can be solved as a limiting case of zero shear modulus of inclusions by using the developed program. Several examples solved previously by other researchers [1–3,6,8–10] were revisited to see the accuracy and efficiency of the present formulation. In addition, the test of convergence is done and the boundary-layer effect for boundary stress is also addressed.

2 Problem Statement

The displacement field of the antiplane deformation is defined as

$$u = v = 0, \quad w = w(x,y), \tag{1}$$

where w is the only nonvanishing component of displacement with respect to the Cartesian coordinate which is a function of x and y. For a linear elastic body, the stress components are

$$\sigma_{zx} = \mu \frac{\partial w}{\partial x}, \tag{2}$$

$$\sigma_{zy} = \mu \frac{\partial w}{\partial y}, \tag{3}$$

where μ is the shear modulus. The equilibrium equation can be simplified to

$$\frac{\partial \sigma_{zx}}{\partial x} + \frac{\partial \sigma_{zy}}{\partial y} = 0. \tag{4}$$

Thus, we have

$$\frac{\partial^2 w}{\partial x^2} + \frac{\partial^2 w}{\partial y^2} = \nabla^2 w = 0. \tag{5}$$

Equation (5) indicates that the governing equation of this problem is the Laplace equation. We consider an infinite medium subject to N circular inclusions bounded by the B_k contour $(k=1,2,\ldots,N)$ for either matrix or inclusions under the antiplane shear σ_{zx}^{∞} and σ_{zy}^{∞} at infinity or equivalently under the displacement $w^{\infty} = \sigma_{zx}^{\infty} x/\mu + \sigma_{zy}^{\infty} y/\mu$ as shown in Fig. 1(a). By taking the free body along the interface between the matrix and inclusions, the problem can be decomposed into two systems. One is an infinite medium with N circular holes under the remote shear and the other is N circular inclusions bounded by the B_k contour which satisfies the Laplace equation as shown in Figs. 1(b) and 1(c), respectively. From the numerical point of view, this is the so-called multidomain approach. For the problem in Fig. 1(b), it can be superimposed by two parts. One is an infinite medium under the remote shear and the other is an infinite medium with N circular holes which satisfies the Laplace equation as shown in Figs. 1(d) and 1(e), respectively. This part was solved efficiently by Chen et al. [18] and the null-field equation approach is adapted here again. Therefore, one exterior problem for the matrix is shown in Fig. 1(e) and several interior problems for nonoverlapping inclusions are shown in Fig. 1(c). According to the null-field integral formulation in Ref. [18], the two problems in Figs. 1(e) and 1(c) can be solved in a unified manner since they both satisfy the Laplace equation.

3 A Unified Formulation for Exterior and Interior Problems

3.1 Dual Boundary Integral Equations and Dual Null-Field Integral Equations. The boundary integral equation for the domain point can be derived from the third Green's identity [20], we have

$$2\pi w(x) = \int_B T(s,x) w(s) dB(s) - \int_B U(s,x) t(s) dB(s), \quad x \in D, \tag{6}$$

$$2\pi \frac{\partial w(x)}{\partial n_x} = \int_B M(s,x) w(s) dB(s) - \int_B L(s,x) t(s) dB(s), \quad x \in D, \tag{7}$$

where $t(s) = \partial w(s)/\partial n_s$, s and x are the source and field points, respectively, B is the boundary, D is the domain of interest, n_s and n_x denote the outward normal vector at the source point s and field point x, respectively, and the kernel function $U(s,x) = \ln r$, $(r \equiv |x-s|)$, is the fundamental solution which satisfies

$$\nabla^2 U(s,x) = 2\pi \delta(x-s), \tag{8}$$

in which $\delta(x-s)$ denotes the Dirac-delta function. The other kernel functions, $T(s,x)$, $L(s,x)$, and $M(s,x)$, are defined by

$$T(s,x) \equiv \frac{\partial U(s,x)}{\partial n_s}, \quad L(s,x) \equiv \frac{\partial U(s,x)}{\partial n_x}, \quad M(s,x) \equiv \frac{\partial^2 U(s,x)}{\partial n_s \partial n_x}. \tag{9}$$

By collocating x outside the domain $(x \in D^c)$, we obtain the dual null-field integral equations as shown below

$$0 = \int_B T(s,x) w(s) dB(s) - \int_B U(s,x) t(s) dB(s), \quad x \in D^c, \tag{10}$$

$$0 = \int_B M(s,x) w(s) dB(s) - \int_B L(s,x) t(s) dB(s), \quad x \in D^c, \tag{11}$$

where D^c is the complementary domain. Based on the separable property, the kernel function $U(s,x)$ is expanded into the degenerate form by separating the source point and field point in the polar coordinate [21]

$$U(s,x) = \begin{cases} U^i(R,\theta;\rho,\phi) = \ln R - \displaystyle\sum_{m=1}^{\infty} \frac{1}{m}\left(\frac{\rho}{R}\right)^m \cos m(\theta-\phi), & R \geqslant \rho \\ U^e(R,\theta;\rho,\phi) = \ln \rho - \displaystyle\sum_{m=1}^{\infty} \frac{1}{m}\left(\frac{R}{\rho}\right)^m \cos m(\theta-\phi), & \rho > R \end{cases}, \tag{12}$$

where the superscripts "i" and "e" denote the interior $(R > \rho)$ and exterior $(\rho > R)$ cases, respectively. The origin of the observer system for the degenerate kernel is (0,0). Figure 2 shows the graph of separate expressions of fundamental solutions where

PROOF COPY [JAM-05-1418] 008606AMJ

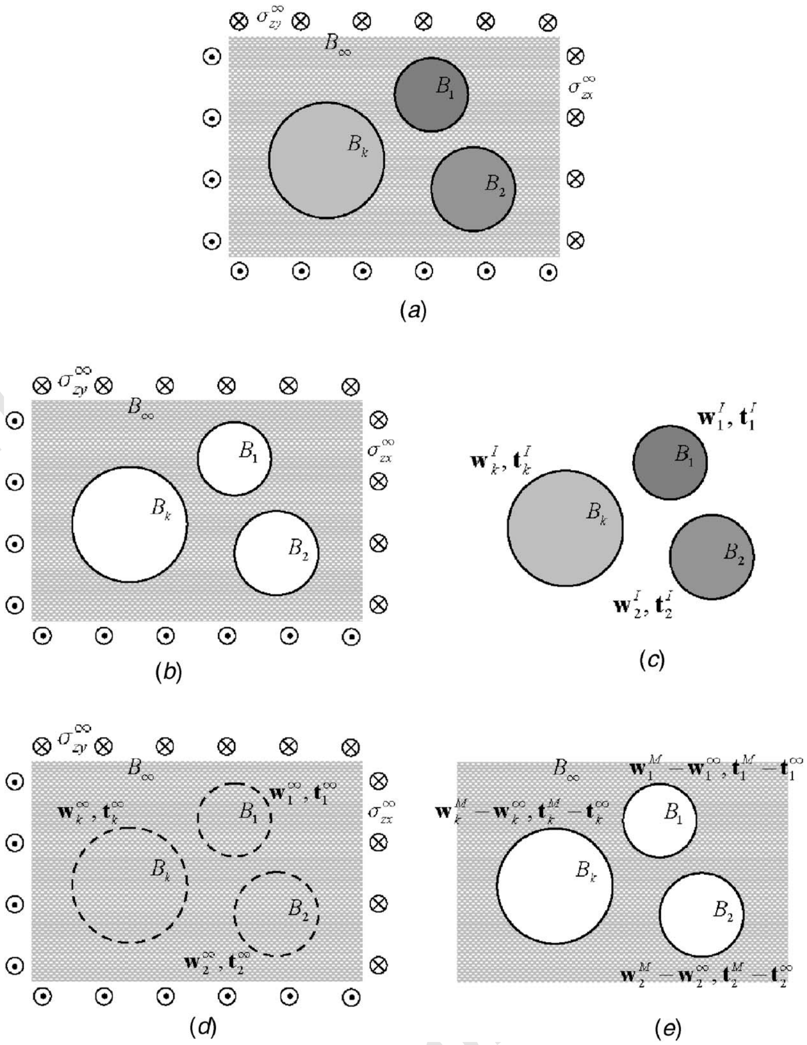

Fig. 1 (*a*) Infinite antiplane problem with arbitrary circular inclusions under the remote shear, (*b*) infinite medium with circular holes under the remote shear, (*c*) interior Laplace problems for each inclusion, (*d*) infinite medium under the remote shear, and (*e*) exterior Laplace problems for the matrix

source point s located at $R=10.0$ and $\theta=\pi/3$. By setting the origin at o for the observer system, a circle with radius R from the origin o to the source point s is plotted. If the field point x is situated inside the circular region, the degenerate kernel belongs to the interior expression of U^i; otherwise, it is the exterior case. After taking the normal derivative $\partial/\partial R$ with respect to Eq. (12), the $T(s,x)$ kernel yields

$$T(s,x) = \begin{cases} T^i(R,\theta;\rho,\phi) = \dfrac{1}{R} + \displaystyle\sum_{m=1}^{\infty}\left(\dfrac{\rho^m}{R^{m+1}}\right)\cos m(\theta-\phi), & R > \rho \\ T^e(R,\theta;\rho,\phi) = -\displaystyle\sum_{m=1}^{\infty}\left(\dfrac{R^{m-1}}{\rho^m}\right)\cos m(\theta-\phi), & \rho > R \end{cases}, \tag{13}$$

and the higher-order kernel functions, $L(s,x)$ and $M(s,x)$, are shown below

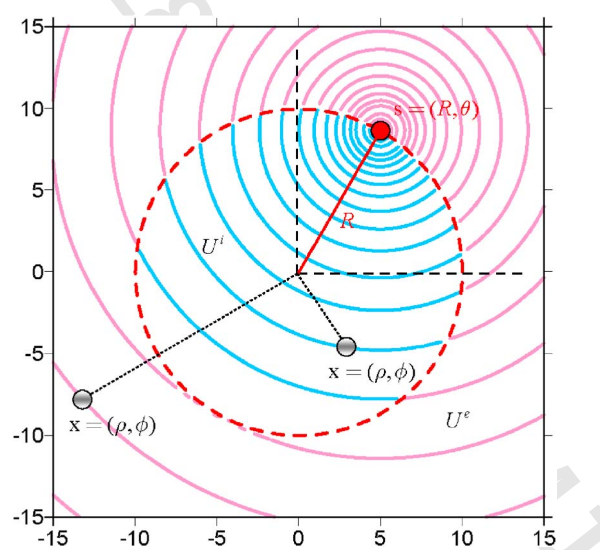

Fig. 2 Graph of the degenerate kernel for the fundamental solution, *s*=(10, π/3)

PROOF COPY [JAM-05-1418] 008606AMJ

$$L(s,x) = \begin{cases} L^i(R,\theta;\rho,\phi) = -\sum_{m=1}^{\infty} \left(\frac{\rho^{m-1}}{R^m}\right)\cos m(\theta-\phi), & R > \rho \\ L^e(R,\theta;\rho,\phi) = \frac{1}{\rho} + \sum_{m=1}^{\infty} \left(\frac{R^m}{\rho^{m+1}}\right)\cos m(\theta-\phi), & \rho > R \end{cases}, \tag{14}$$

$$M(s,x) = \begin{cases} M^i(R,\theta;\rho,\phi) = \sum_{m=1}^{\infty} \left(\frac{m\rho^{m-1}}{R^{m+1}}\right)\cos m(\theta-\phi), & R \geqslant \rho \\ M^e(R,\theta;\rho,\phi) = \sum_{m=1}^{\infty} \left(\frac{mR^{m-1}}{\rho^{m+1}}\right)\cos m(\theta-\phi), & \rho > R \end{cases}. \tag{15}$$

Since the potentials resulted from $T(s,x)$ and $L(s,x)$ kernels are discontinuous across the boundary, the potentials of $T(s,x)$ and $L(s,x)$ for $R\to\rho^+$ and $R\to\rho^-$ are different. This is the reason why $R=\rho$ is not included for degenerate kernels of $T(s,x)$ and $L(s,x)$ in Eqs. (13) and (14). For problems with circular boundaries, we apply the Fourier series expansions to approximate the potential w and its normal derivative t on the boundary as

$$w(s_k) = a_0^k + \sum_{n=1}^{L} (a_n^k \cos n\theta_k + b_n^k \sin n\theta_k),$$

$$s_k \in B_k, \quad k = 0,1,2,\ldots,N, \tag{16}$$

$$t(s_k) = p_0^k + \sum_{n=1}^{L} (p_n^k \cos n\theta_k + q_n^k \sin n\theta_k),$$

$$s_k \in B_k, \quad k = 0,1,2,\ldots,N, \tag{17}$$

where $t(s_k)=\partial w(s_k)/\partial n_s$, a_n^k, b_n^k, p_n^k and q_n^k $(n=0,1,2,\ldots)$ are the Fourier coefficients and θ_k is the polar angle. In the real computation, only $2L+1$ finite terms are considered where L indicates the truncated terms of Fourier series.

3.2 Adaptive Observer System [18,19]. By using the collocation method, the null-field integral equation becomes a set of algebraic equations for the Fourier coefficients. To ensure the stability of the algebraic equations, one has to choose collocating points throughout all the circular boundaries of the inclusions. Since the boundary integral equation is derived from the reciprocal theorem of energy concept. Therefore, the boundary integral equation is frame indifferent due to the objectivity rule. This is the reason why the observer system is adaptively to locate the origin at the center of circle in the boundary integration. The adaptive observer system is chosen to fully employ the property of degenerate kernels. Figures 3(*a*) and 3(*b*) show the boundary integration for the circular boundary in the adaptive observer system. It is worth noting that the origin of the observer system is located on the center of the corresponding circle under integration to entirely utilize the geometry of circular boundary for the expansion of degenerate kernels and boundary densities. The dummy variable in the circular integration is the angle (θ) instead of the radial coordinate (R).

3.3 Linear Algebraic System. By moving the null-field point x_j to the jth circular boundary in the limit sense for Eq. (10) in Fig. 3(*a*), we have

$$0 = \sum_{k=0}^{N} \int_{B_k} T(R_k,\theta_k;\rho_j,\phi_j) w(R_k,\theta_k) R_k d\theta_k - \sum_{k=0}^{N} \int_{B_k} U(R_k,\theta_k;\rho_j,\phi_j) t(R_k,\theta_k) R_k d\theta_k, \ x(\rho_j,\phi_j) \in D^c, \tag{18}$$

where N is the number of circular inclusions and B_0 denotes the outer boundary for the bounded domain. In case of the infinite problem, B_0 becomes B_∞. Note that the kernels $U(s,x)$ and $T(s,x)$ are assumed in the degenerate form given by Eqs. (12) and (13), respectively, while the boundary densities w and t are expressed in terms of the Fourier series expansion forms given by Eqs. (16) and (17), respectively. Then, the integrals multiplied by separate expansion coefficients in Eq. (18) are nonsingular and the limit of the null-field point to the boundary is easily implemented by using appropriate forms of degenerate kernels. Through such an idea, all the singular and hypersingular integrals are well captured. Thus, the collocation point $x(\rho_j,\phi_j)$ in the discretized Eq. (18) can be considered on the boundary B_j, as well as the null-field point. Along each circular boundary, $2L+1$ collocation points are required to match $2L+1$ terms of Fourier series for constructing a square influence matrix with the dimension of $2L+1$ by $2L+1$. In contrast to the standard discretized boundary integral equation formulation with nodal unknowns of the physical boundary densities w and t. Now the degrees of freedom are transformed to Fourier coefficients employed in expansion of boundary densities. It is found that the compatible relationship of the boundary unknowns is equivalent by moving either the null-field point or the domain point to the boundary in different directions using various degenerate kernels as shown in Figs. 3(*a*) and 3(*b*). In the B_k integration, we set the origin of the observer system to collocate at the center c_k to fully utilize the degenerate kernels and Fourier series. By collocating the null-field point on the boundary, the linear algebraic system is obtained.

For the exterior problem of matrix, we have

$$[\mathbf{U}^M]\{\mathbf{t}^M - \mathbf{t}^\infty\} = [\mathbf{T}^M]\{\mathbf{w}^M - \mathbf{w}^\infty\}. \tag{19}$$

For the interior problem of each inclusion, we have

$$[\mathbf{U}^I]\{\mathbf{t}^I\} = [\mathbf{T}^I]\{\mathbf{w}^I\}, \tag{20}$$

where the superscripts "M" and "I" denote the matrix and inclusion, respectively. $[\mathbf{U}^M]$, $[\mathbf{T}^M]$, $[\mathbf{U}^I]$, and $[\mathbf{T}^I]$ are the influence matrices with a dimension of $(N+1)(2L+1)$ by $(N+1)(2L+1)$, $\{\mathbf{w}^M\}$, $\{\mathbf{t}^M\}$, $\{\mathbf{w}^\infty\}$, $\{\mathbf{t}^\infty\}$, $\{\mathbf{w}^I\}$, and $\{\mathbf{t}^I\}$ denote the column vectors of Fourier coefficients with a dimension of $(N+1)(2L+1)$ by 1 in which those are defined as follows:

$$[\mathbf{U}^M] = \begin{bmatrix} \mathbf{U}_{00}^M & \mathbf{U}_{01}^M & \cdots & \mathbf{U}_{0N}^M \\ \mathbf{U}_{10}^M & \mathbf{U}_{11}^M & \cdots & \mathbf{U}_{1N}^M \\ \vdots & \vdots & \ddots & \vdots \\ \mathbf{U}_{N0}^M & \mathbf{U}_{N1}^M & \cdots & \mathbf{U}_{NN}^M \end{bmatrix},$$

$$[\mathbf{T}^M] = \begin{bmatrix} \mathbf{T}_{00}^M & \mathbf{T}_{01}^M & \cdots & \mathbf{T}_{0N}^M \\ \mathbf{T}_{10}^M & \mathbf{T}_{11}^M & \cdots & \mathbf{T}_{1N}^M \\ \vdots & \vdots & \ddots & \vdots \\ \mathbf{T}_{N0}^M & \mathbf{T}_{N1}^M & \cdots & \mathbf{T}_{NN}^M \end{bmatrix}, \tag{21}$$

$$[\mathbf{U}^I]=\begin{bmatrix}\mathbf{U}^I_{00} & \mathbf{U}^I_{01} & \cdots & \mathbf{U}^I_{0N}\\ \mathbf{U}^I_{10} & \mathbf{U}^I_{11} & \cdots & \mathbf{U}^I_{1N}\\ \vdots & \vdots & \ddots & \vdots\\ \mathbf{U}^I_{N0} & \mathbf{U}^I_{N1} & \cdots & \mathbf{U}^I_{NN}\end{bmatrix},\quad [\mathbf{T}^I]=\begin{bmatrix}\mathbf{T}^I_{00} & \mathbf{T}^I_{01} & \cdots & \mathbf{T}^I_{0N}\\ \mathbf{T}^I_{10} & \mathbf{T}^I_{11} & \cdots & \mathbf{T}^I_{1N}\\ \vdots & \vdots & \ddots & \vdots\\ \mathbf{T}^I_{N0} & \mathbf{T}^I_{N1} & \cdots & \mathbf{T}^I_{NN}\end{bmatrix}, \tag{22}$$

$$\{\mathbf{w}^M\}=\begin{Bmatrix}\mathbf{w}^M_0\\ \mathbf{w}^M_1\\ \mathbf{w}^M_2\\ \vdots\\ \mathbf{w}^M_N\end{Bmatrix},\quad \{\mathbf{t}^M\}=\begin{Bmatrix}\mathbf{t}^M_0\\ \mathbf{t}^M_1\\ \mathbf{t}^M_2\\ \vdots\\ \mathbf{t}^M_N\end{Bmatrix}, \tag{23}$$

$$\{\mathbf{w}^\infty\}=\begin{Bmatrix}\mathbf{w}^\infty_0\\ \mathbf{w}^\infty_1\\ \mathbf{w}^\infty_2\\ \vdots\\ \mathbf{w}^\infty_N\end{Bmatrix},\quad \{\mathbf{t}^\infty\}=\begin{Bmatrix}\mathbf{t}^\infty_0\\ \mathbf{t}^\infty_1\\ \mathbf{t}^\infty_2\\ \vdots\\ \mathbf{t}^\infty_N\end{Bmatrix}, \tag{24}$$

$$\{\mathbf{w}^I\}=\begin{Bmatrix}\mathbf{w}^I_0\\ \mathbf{w}^I_1\\ \mathbf{w}^I_2\\ \vdots\\ \mathbf{w}^I_N\end{Bmatrix},\quad \{\mathbf{t}^I\}=\begin{Bmatrix}\mathbf{t}^I_0\\ \mathbf{t}^I_1\\ \mathbf{t}^I_2\\ \vdots\\ \mathbf{t}^I_N\end{Bmatrix}, \tag{25}$$

where $\{\mathbf{w}^M\}$, $\{\mathbf{t}^M\}$, $\{\mathbf{w}^\infty\}$, $\{\mathbf{t}^\infty\}$, $\{\mathbf{w}^I\}$, and $\{\mathbf{t}^I\}$ are the vectors of Fourier coefficients and the first subscript "j" ($j=0,1,2,\cdots,N$) in $[\mathbf{U}^M_{jk}]$, $[\mathbf{T}^M_{jk}]$, $[\mathbf{U}^I_{jk}]$, and $[\mathbf{T}^I_{jk}]$ denotes the index of the jth circle where the collocation point is located and the second subscript "k" ($k=0,1,2,\ldots,N$) denotes the index of the kth circle when integrating on each boundary data $\{\mathbf{w}^M_k-\mathbf{w}^\infty_k\}$, $\{\mathbf{t}^M_k-\mathbf{t}^\infty_k\}$, $\{\mathbf{w}^I_k\}$, and $\{\mathbf{t}^I_k\}$, N is the number of circular inclusions in the domain and the number L indicates the truncated terms of Fourier series. It is noted that $\{\mathbf{w}^\infty\}$ and $\{\mathbf{t}^\infty\}$ in Fig. 1(d) are the displacement and traction due to the remote shear. The coefficient matrix of the linear algebraic system is partitioned into blocks, and each off-diagonal block corresponds to the influence matrices between two different circular boundaries. The diagonal blocks are the influence matrices due to itself in each individual circle. After uniformly collocating the point along the kth circular boundary, the submatrix can be written as

$$[\mathbf{U}^M_{jk}]=\begin{bmatrix}U^{0c}_{jk}(\phi_1) & U^{1c}_{jk}(\phi_1) & U^{1s}_{jk}(\phi_1) & \cdots & U^{Lc}_{jk}(\phi_1) & U^{Ls}_{jk}(\phi_1)\\ U^{0c}_{jk}(\phi_2) & U^{1c}_{jk}(\phi_2) & U^{1s}_{jk}(\phi_2) & \cdots & U^{Lc}_{jk}(\phi_2) & U^{Ls}_{jk}(\phi_2)\\ U^{0c}_{jk}(\phi_3) & U^{1c}_{jk}(\phi_3) & U^{1s}_{jk}(\phi_3) & \cdots & U^{Mc}_{jk}(\phi_3) & U^{Ls}_{jk}(\phi_3)\\ \vdots & \vdots & \vdots & \ddots & \vdots & \vdots\\ U^{0c}_{jk}(\phi_{2L}) & U^{1c}_{jk}(\phi_{2L}) & U^{1s}_{jk}(\phi_{2L}) & \cdots & U^{Lc}_{jk}(\phi_{2L}) & U^{Ls}_{jk}(\phi_{2L})\\ U^{0c}_{jk}(\phi_{2L+1}) & U^{1c}_{jk}(\phi_{2L+1}) & U^{1s}_{jk}(\phi_{2L+1}) & \cdots & U^{Lc}_{jk}(\phi_{2L+1}) & U^{Ls}_{jk}(\phi_{2L+1})\end{bmatrix}, \tag{26}$$

$$[\mathbf{T}^M_{jk}]=\begin{bmatrix}T^{0c}_{jk}(\phi_1) & T^{1c}_{jk}(\phi_1) & T^{1s}_{jk}(\phi_1) & \cdots & T^{Lc}_{jk}(\phi_1) & T^{Ls}_{jk}(\phi_1)\\ T^{0c}_{jk}(\phi_2) & T^{1c}_{jk}(\phi_2) & T^{1s}_{jk}(\phi_2) & \cdots & T^{Lc}_{jk}(\phi_2) & T^{Ls}_{jk}(\phi_2)\\ T^{0c}_{jk}(\phi_3) & T^{1c}_{jk}(\phi_3) & T^{1s}_{jk}(\phi_3) & \cdots & T^{Lc}_{jk}(\phi_3) & T^{Ls}_{jk}(\phi_3)\\ \vdots & \vdots & \vdots & \ddots & \vdots & \vdots\\ T^{0c}_{jk}(\phi_{2L}) & T^{1c}_{jk}(\phi_{2L}) & T^{1s}_{jk}(\phi_{2L}) & \cdots & T^{Lc}_{jk}(\phi_{2L}) & T^{Ls}_{jk}(\phi_{2L})\\ T^{0c}_{jk}(\phi_{2L+1}) & T^{1c}_{jk}(\phi_{2L+1}) & T^{1s}_{jk}(\phi_{2L+1}) & \cdots & T^{Lc}_{jk}(\phi_{2L+1}) & T^{Ls}_{jk}(\phi_{2L+1})\end{bmatrix}, \tag{27}$$

where ϕ_j, $j=1,2,\ldots,2L+1$, is the angle of collocation point along the circular boundary. Although both the matrices in Eqs. (26) and (27) are not sparse, it is found that the higher order harmonics, the lower influence coefficients in numerical experiments. It is noted that the superscript "$0s$" in Eqs. (26) and (27) disappears since $\sin\theta=0$. The element of $[\mathbf{U}^M_{jk}]$ and $[\mathbf{T}^M_{jk}]$ are defined, respectively, as

$$U^{nc}_{jk}(\phi_m)=\int_{B_k}U(s_k,x_m)\cos(n\theta_k)R_k d\theta_k,\quad n=0,1,2,\ldots,L,$$

$$(28)\, m=1,2,\ldots,2L+1,$$

$$U^{ns}_{jk}(\phi_m)=\int_{B_k}U(s_k,x_m)\sin(n\theta_k)R_k d\theta_k,$$

$$n=1,2,\ldots,L,\quad m=1,2,\ldots,2L+1, \tag{29}$$

$$T^{ns}_{jk}(\phi_m)=\int_{B_k}T(s_k,x_m)\cos(n\theta_k)R_k d\theta_k,$$

$$n=0,1,2,\ldots,L,\quad m=1,2,\ldots,2L+1, \tag{30}$$

$$T^{ns}_{jk}(\phi_m)=\int_{B_k}T(s_k,x_m)\sin(n\theta_k)R_k d\theta_k,$$

$$n=1,2,\ldots,L,\quad m=1,2,\ldots,2L+1, \tag{31}$$

where k is no sum, $S_k=(R_k,\theta_k)$, and ϕ_m is the angle of collocation point X_m along the boundary. The submatrix $[\mathbf{U}^I_{jk}]$ and $[\mathbf{T}^I_{jk}]$ can be written in a similar way. Equation (18) can be calculated by employing the orthogonal property of trigonometric function in the real computation. Only the finite L terms are used in the summation of Eqs. (16) and (17). The explicit forms of all the boundary integrals for U, T, L, and M kernels are listed in the Table 1.

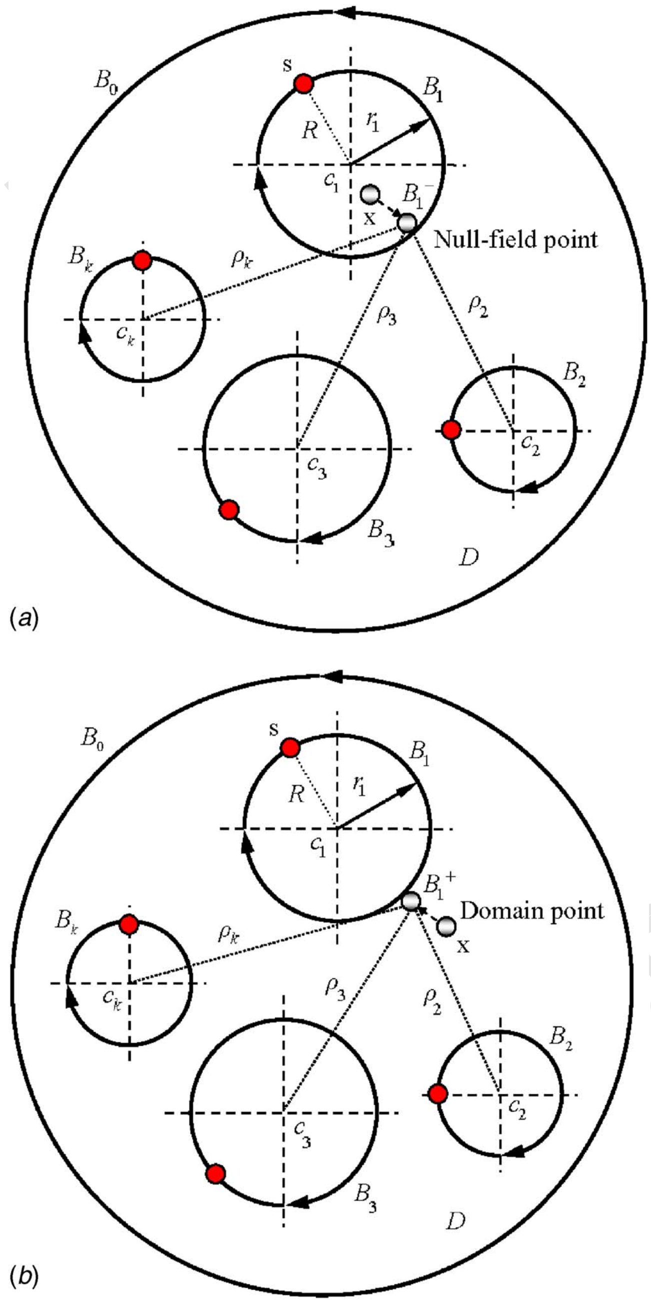

Fig. 3 (*a*) **Sketch of the null-field integral equation for a null-field point in conjunction with the adaptive observer system** ($x \notin D, x \to B_k$) **and** (*b*) **sketch of the boundary integral equation for a domain point in conjunction with the adaptive observer system** ($x \in D, x \to B_k$)

Finite values of singular and hypersingular integrals are well captured after introducing the degenerate kernel. Besides, the limiting case across the boundary ($R^- \to \rho \to R^+$) is also addressed. The continuous and jump behavior across the boundary is well described. Instead of boundary data in the BEM, the Fourier coefficients become the new unknown degrees of freedom in the formulation. Two cases may be solved in a unified manner using the null-field integral formulation:

(1) One bounded problem of the circular domain in Fig. 1(*c*) becomes the interior problem for each inclusion.
(2) The other is unbounded, i.e., the outer boundary B_0 in Fig. 3(*a*) is B_∞. It is the exterior problem for the matrix as shown in Fig. 1(*e*).

The direction of contour integration should be taken care, i.e., counterclockwise and clockwise directions are for the interior and exterior problems, respectively.

3.4 Match of Interface Conditions. According to the continuity of displacement and equilibrium of traction along the kth interface, we have the two constraints

$$\{\mathbf{w}^M\} = \{\mathbf{w}^I\} \quad \text{on } B_k, \tag{32}$$

$$[\boldsymbol{\mu}_0]\{\mathbf{t}^M\} = -[\boldsymbol{\mu}_\mathbf{k}]\{\mathbf{t}^I\} \quad \text{on } B_k, \tag{33}$$

where $[\boldsymbol{\mu}_0]$ and $[\boldsymbol{\mu}_\mathbf{k}]$ are defined as follows:

$$[\boldsymbol{\mu}_0] = \begin{bmatrix} \mu_0 & 0 & \cdots & 0 \\ 0 & \mu_0 & \cdots & 0 \\ \vdots & \vdots & \ddots & \vdots \\ 0 & 0 & \cdots & \mu_0 \end{bmatrix}, \quad [\boldsymbol{\mu}_\mathbf{k}] = \begin{bmatrix} \mu_k & 0 & \cdots & 0 \\ 0 & \mu_k & \cdots & 0 \\ \vdots & \vdots & \ddots & \vdots \\ 0 & 0 & \cdots & \mu_k \end{bmatrix}, \tag{34}$$

where μ_0 and μ_k denote the shear modulus of the matrix and the kth inclusion, respectively. By assembling the matrices in Eqs. (19), (20), (32), and (33), we have

$$\begin{bmatrix} \mathbf{T}^M & -\mathbf{U}^M & \mathbf{0} & \mathbf{0} \\ \mathbf{0} & \mathbf{0} & \mathbf{T}^I & -\mathbf{U}^I \\ \mathbf{I} & \mathbf{0} & -\mathbf{I} & \mathbf{0} \\ \mathbf{0} & \boldsymbol{\mu}_\mathbf{0} & \mathbf{0} & \boldsymbol{\mu}_\mathbf{k} \end{bmatrix} \begin{Bmatrix} \mathbf{w}^M \\ \mathbf{t}^M \\ \mathbf{w}^I \\ \mathbf{t}^I \end{Bmatrix} = \begin{Bmatrix} \mathbf{a} \\ \mathbf{0} \\ \mathbf{0} \\ \mathbf{0} \end{Bmatrix}, \tag{35}$$

where $\{\mathbf{a}\}$ is the forcing term due to the remote shear stress and $[\mathbf{I}]$ is the identity matrix. The calculation for the vector $\{\mathbf{a}\}$ is elaborated on later in Appendix A. After obtaining the unknown Fourier coefficients in Eq. (35), the origin of observer system is set to c_k in the B_k integration as shown in Fig. 3(*b*) to obtain the field potential by employing Eq. (6). The differences between the present formulation and the conventional BEM are listed in Table 2.

3.5 Vector Decomposition Technique for the Potential Gradient in the Hypersingular Equation. In order to determine the stress field, the tangential derivative should be calculated with care. Also Eq. (7) shows the normal derivative of potential for domain points. For the nonconcentric cases, special treatment for the potential gradient should be considered as the source point and field point locate on different circular boundaries. As shown in Fig. 4, the normal direction on the boundary (1, 1′) should be superimposed by those of the radial derivative (3, 3′) and angular derivative (4, 4′) through the vector decomposition technique. According to the concept of vector decomposition technique, the kernel functions of Eqs. (14) and (15) can be modified to

$$L(,) = \begin{cases} L^i(R,\theta;\rho,\phi) = -\displaystyle\sum_{m=1}^{\infty}\left(\frac{\rho^{m-1}}{R^m}\right)\cos m(\theta-\phi)\cos(\zeta-\xi) - \sum_{m=1}^{\infty}\left(\frac{\rho^{m-1}}{R^m}\right)\sin m(\theta-\phi)\cos\left(\frac{\pi}{2}-\zeta+\xi\right), & R>\rho \\ L^e(R,\theta;\rho,\phi) = \dfrac{1}{\rho} + \displaystyle\sum_{m=1}^{\infty}\left(\frac{R^m}{\rho^{m+1}}\right)\cos m(\theta-\phi)\cos(\zeta-\xi) - \sum_{m=1}^{\infty}\left(\frac{R^m}{\rho^{m+1}}\right)\sin m(\theta-\phi)\cos\left(\frac{\pi}{2}-\zeta+\xi\right), & \rho>R \end{cases}, \tag{36}$$

Table 1 Influence coefficients for the singularity distribution on the circular boundary

		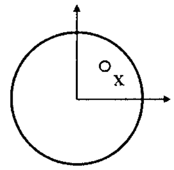 $\rho<R$		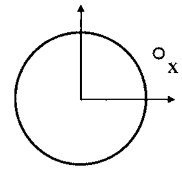 $\rho>R$
$U(\mathrm{s},\mathrm{x})$	Degenerate kernel	$U^i(R,\theta;\rho,\phi)=\ln R-\sum_{m=1}^{\infty}\frac{1}{m}(\frac{\rho}{R})^m\cos m(\theta-\phi),\ R\ge\rho$		$U^e(R,\theta;\rho,\phi)=\ln\rho-\sum_{m=1}^{\infty}\frac{1}{m}(\frac{R}{\rho})^m\cos m(\theta-\phi),\ \rho>R$
	Orthogonal process	$\int_0^{2\pi}[U^i][1]Rd\theta=2\pi\ln R,\ R\ge\rho$ $\int_0^{2\pi}[U^i][\cos n\theta]Rd\theta=\pi\frac{1}{n}\frac{\rho^n}{R^{n-1}}\cos n\phi,\ R\ge\rho$ $\int_0^{2\pi}[U^i][\sin n\theta]Rd\theta=\pi\frac{1}{n}\frac{\rho^n}{R^{n-1}}\sin n\phi,\ R\ge\rho$		$\int_0^{2\pi}[U^e][1]Rd\theta=2\pi\ln\rho,\ \rho>R$ $\int_0^{2\pi}[U^e][\cos n\theta]Rd\theta=\pi\frac{1}{n}\frac{R^{n+1}}{\rho^n}\cos n\phi,\ \rho>R$ $\int_0^{2\pi}[U^e][\sin n\theta]Rd\theta=\pi\frac{1}{n}\frac{R^{n+1}}{\rho^n}\sin n\phi,\ \rho>R$
	Limiting behavior across the boundary	$\lim_{\rho\to R}2\pi\ln R=2\pi\ln R$ $\lim_{\rho\to R}\pi\frac{1}{n}\frac{\rho^n}{R^{n-1}}\cos n\phi=\pi\frac{1}{n}R\cos n\phi$ $\lim_{\rho\to R}\pi\frac{1}{n}\frac{\rho^n}{R^{n-1}}\sin n\phi=\pi\frac{1}{n}R\sin n\phi$	Continuous $(R^-\to R\to R^+)$	$\lim_{\rho\to R}2\pi\ln\rho=2\pi\ln R$ $\lim_{\rho\to R}\pi\frac{1}{n}\frac{R^{n+1}}{\rho^n}\cos n\phi=\pi\frac{1}{n}R\cos n\phi$ $\lim_{\rho\to R}\pi\frac{1}{n}\frac{R^{n+1}}{\rho^n}\sin n\phi=\pi\frac{1}{n}R\sin n\phi$
$T(\mathrm{s},\mathrm{x})$	Degenerate kernel	$T^i(R,\theta;\rho,\phi)=\frac{1}{R}+\sum_{m=1}^{\infty}(\frac{\rho^m}{R^{m+1}})\cos m(\theta-\phi),\ \ R>\rho$		$T^e(R,\theta;\rho,\phi)=-\sum_{m=1}^{\infty}(\frac{R^{m-1}}{\rho^m})\cos m(\theta-\phi),\ \ \rho>R$
	Orthogonal process	$\int_0^{2\pi}[T^i][1]Rd\theta=\frac{2\pi}{R},\ R>\rho$ $\int_0^{2\pi}[T^i][\cos n\theta]Rd\theta=\pi(\frac{\rho}{R})^n\cos n\phi,\ R>\rho$ $\int_0^{2\pi}[T^i][\sin n\theta]Rd\theta=\pi(\frac{\rho}{R})^n\sin n\phi,\ R>\rho$		$\int_0^{2\pi}[T^e][1]Rd\theta=0,\ \rho>R$ $\int_0^{2\pi}[T^e][\cos n\theta]Rd\theta=-\pi(\frac{R}{\rho})^n\cos n\phi,\ \rho>R$ $\int_0^{2\pi}[T^e][\sin n\theta]Rd\theta=-\pi(\frac{R}{\rho})^n\sin n\phi,\ \rho>R$
	Limiting behavior across the boundary	$\lim_{\rho\to R}\frac{2\pi}{R}=\frac{2\pi}{R}$ $\lim_{\rho\to R}\pi(\frac{\rho}{R})^n\cos n\phi=\pi\cos n\phi$ $\lim_{\rho\to R}\pi(\frac{\rho}{R})^n\sin n\phi=\pi\sin n\phi$	Jump $(R^-\to R\to R^+)$	$\lim_{\rho\to R}0=0$ $\lim_{\rho\to R}-\pi(\frac{R}{\rho})^n\cos n\phi=-\pi\cos n\phi$ $\lim_{\rho\to R}-\pi(\frac{R}{\rho})^n\sin n\phi=-\pi\sin n\phi$

$$M(,)=\begin{cases}M^i(R,\theta;\rho,\phi)=\sum_{m=1}^{\infty}\left(\frac{m\rho^{m-1}}{R^{m+1}}\right)\cos m(\theta-\phi)\cos(\zeta-\xi)-\sum_{m=1}^{\infty}\left(\frac{m\rho^{m-1}}{R^{m+1}}\right)\sin m(\theta-\phi)\cos\left(\frac{\pi}{2}-\zeta+\xi\right), & R\geqslant\rho\\ M^e(R,\theta;\rho,\phi)=\sum_{m=1}^{\infty}\left(\frac{mR^{m-1}}{\rho^{m+1}}\right)\cos m(\theta-\phi)\cos(\zeta-\xi)-\sum_{m=1}^{\infty}\left(\frac{mR^{m-1}}{\rho^{m+1}}\right)\sin m(\theta-\phi)\cos\left(\frac{\pi}{2}-\zeta+\xi\right), & \rho>R\end{cases}\tag{37}$$

where ζ and ξ are shown in Fig. 4. For the special case of confocal, the potential gradient is derived free of special treatment since $\zeta=\xi$.

3.6 Stresses Described in the Polar Coordinate. After obtaining all the unknown Fourier coefficients of w and t for the matrix and inclusions, the stress described in the polar coordinate

Table 1 (*Continued.*)

		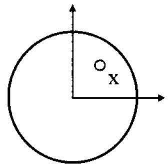 $\rho < R$		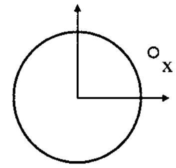 $\rho > R$
$L(\mathrm{s},\mathrm{x})$	Degenerate kernel	$L^i(R,\theta;\rho,\phi) = -\sum_{m=1}^{\infty}(\frac{\rho^{m-1}}{R^m})\cos m(\theta-\phi),\ R>\rho$		$L^e(R,\theta;\rho,\phi) = \frac{1}{\rho}+\sum_{m=1}^{\infty}(\frac{R^m}{\rho^{m+1}})\cos m(\theta-\phi),\ \rho>R$
	Orthogonal process	$\int_0^{2\pi}[L^i][1]Rd\theta = 0,\ R>\rho$ $\int_0^{2\pi}[L^i][\cos n\theta]Rd\theta = -\pi(\frac{\rho}{R})^{n-1}\cos n\phi,\ R>\rho$ $\int_0^{2\pi}[L^i][\sin n\theta]Rd\theta = -\pi(\frac{\rho}{R})^{n-1}\sin n\phi,\ R>\rho$		$\int_0^{2\pi}[L^e][1]Rd\theta = \frac{2\pi}{\rho},\ \rho>R$ $\int_0^{2\pi}[L^e][\cos n\theta]Rd\theta = \pi(\frac{R}{\rho})^{n+1}\cos n\phi,\ \rho>R$ $\int_0^{2\pi}[L^e][\sin n\theta]Rd\theta = \pi(\frac{R}{\rho})^{n+1}\sin n\phi,\ \rho>R$
	Limiting behavior across the boundary	$\lim_{\rho\to R} 0 = 0$ $\lim_{\rho\to R} -\pi(\frac{\rho}{R})^{n-1}\cos n\phi = -\pi\cos n\phi$ $\lim_{\rho\to R} -\pi(\frac{\rho}{R})^{n-1}\sin n\phi = -\pi\sin n\phi$	Jump $(R^- \to R \to R^+)$	$\lim_{\rho\to R}\frac{2\pi}{\rho} = \frac{2\pi}{R}$ $\lim_{\rho\to R}\pi(\frac{R}{\rho})^{n+1}\cos n\phi = \pi\cos n\phi$ $\lim_{\rho\to R}\pi(\frac{R}{\rho})^{n+1}\sin n\phi = \pi\sin n\phi$
$M(\mathrm{s},\mathrm{x})$	Degenerate kernel	$M^i(R,\theta;\rho,\phi) = \sum_{m=1}^{\infty}(\frac{m\rho^{m-1}}{R^{m+1}})\cos m(\theta-\phi),\ R\ge\rho$		$M^e(R,\theta;\rho,\phi) = \sum_{m=1}^{\infty}(\frac{mR^{m-1}}{\rho^{m+1}})\cos m(\theta-\phi),\ \rho>R$
	Orthogonal process	$\int_0^{2\pi}[M^i][1]Rd\theta = 0,\ R\ge\rho$ $\int_0^{2\pi}[M^i][\cos n\theta]Rd\theta = n\pi\frac{\rho^{n-1}}{R^n}\cos n\phi,\ R\ge\rho$ $\int_0^{2\pi}[M^i][\sin n\theta]Rd\theta = n\pi\frac{\rho^{n-1}}{R^n}\sin n\phi,\ R\ge\rho$		$\int_0^{2\pi}[M^e][1]Rd\theta = 0,\ \rho>R$ $\int_0^{2\pi}[M^e][\cos n\theta]Rd\theta = n\pi\frac{R^n}{\rho^{n+1}}\cos n\phi,\ \rho>R$ $\int_0^{2\pi}[M^e][\sin n\theta]Rd\theta = n\pi\frac{R^n}{\rho^{n+1}}\sin n\phi,\ \rho>R$
	Limiting behavior across the boundary	$\lim_{\rho\to R} 0 = 0$ $\lim_{\rho\to R} n\pi\frac{\rho^{n-1}}{R^n}\cos n\phi = n\pi\frac{1}{R}\cos n\phi$ $\lim_{\rho\to R} n\pi\frac{\rho^{n-1}}{R^n}\sin n\phi = n\pi\frac{1}{R}\sin n\phi$	Continuous $(R^- \to R \to R^+)$	$\lim_{\rho\to R} 0 = 0$ $\lim_{\rho\to R} n\pi\frac{R^n}{\rho^{n+1}}\cos n\phi = n\pi\frac{1}{R}\cos n\phi$ $\lim_{\rho\to R} n\pi\frac{R^n}{\rho^{n+1}}\sin n\phi = n\pi\frac{1}{R}\sin n\phi$

can be determined by

$$\sigma_{zr} = \sigma_{zx}\cos\phi + \sigma_{zy}\sin\phi, \tag{38}$$

$$\sigma_{z\theta} = -\sigma_{zx}\sin\phi + \sigma_{zy}\cos\phi, \tag{39}$$

where σ_{zr} and $\sigma_{z\theta}$ are the normal and tangential stresses, respectively. The boundary integral equation for the domain point including the boundary point instead of the null-field formulation is employed to find the stress by employing the appropriate form of degenerate kernels. The flowchart of the present method is shown in Table 3.

4 Numerical Results and Discussions

First, we derive an exact solution for a single inclusion using the present formulation in Appendix B. Symbolic software of MATHEMATICA is employed to solve a $2L+1$ by $2L+1$ sparse matrix by using the induction concept. Then, seven problems solved by previous scholars are revisited by using the present method to show the generality and validity of our formulation. Besides, we demonstrate the problem of interaction of two cavities in case 1 to compare the present method with the conventional BEM.

4.1 Case 1: Two Equal-Sized Holes Lie on the x Axis (a Limiting Case) [2,9].

Figure 5(a) shows the geometry of two equal-sized holes in the infinite medium under the remote shear

Table 2 Comparisons of the present method and conventional BEM

	Boundary density discretization	Auxiliary system	Formulation	Observer system	Singularity	Convergence	Boundary-layer effect
Present method	Fourier series 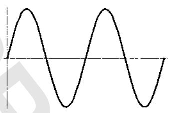	Degenerate kernel	Null-field integral equation	Adaptive observer system	Disappear after introducing the degenerate kernel	Exponential convergence	Free
Conventional BEM	Constant element 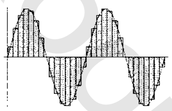	Fundamental solution	Boundary integral equation	Fixed observer system	Principal values ($C.P.V.$, $R.P.V.$ and $H.P.V.$)	Linear algebraic convergence	Appear

where $C.P.V.$, $R.P.V.$ and $H.P.V.$ are the Cauchy, Riemann and Hadamard principal values, respectively.

$\sigma_{zy}^{\infty}=\tau_{\infty}$. The stress concentration of the problem is illustrated in Fig. 5(b). It indicates that the present result agrees well with the analytical solution of Steif [2] and those obtained by Chao and Young [9] even though the two holes approach each other. Figure 5(c) shows that only few terms of Fourier series can obtain good results. However, more nodes are required by using the conventional BEM to achieve convergence. Our formulation is free of boundary-layer effect instead of appearance by using the conventional BEM when the stress $\sigma_{z\theta}$ near the boundary as shown in Fig. 5(d). Stress concentration factors and errors for various distances between two inclusions by using the present method and the conventional BEM are listed in Table 4. These results show that the present method is more accurate and effective than those of the conventional BEM. Under the same error tolerance, the CPU time of the present method is fewer than that of the conventional BEM. Besides, it is noted that more terms of Fourier series are required to capture the singular behavior when the two inclusions approach each other.

4.2 Case 2: Two Identical Inclusions Locating on the x Axis [3]. We consider two identical elastic inclusions of radii $r_1=r_2$ and shear moduli $\mu_1=\mu_2$ embedded in an infinite medium subjected to the remote shear $\sigma_{zx}^{\infty}=\tau_{\infty}$ at infinity as shown in Fig. 6(a). Figure 6(b) shows that stress concentrations diminish when the inclusion spacing increases. We note that the mathematical model of rigid-inclusion problem is equivalent to that of uniform potential flow past two parallel cylinders with no circulation around either cylinder. The remote shear $\sigma_{zx}^{\infty}=\tau_{\infty}$ is similar to the velocity V_{∞} in the x direction at infinity and the velocity field is similar to the stress field [22].

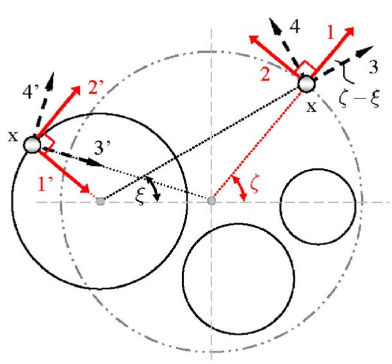

Fig. 4 Vector decomposition for the potential gradient in the hypersingular equation

4.3 Case 3: Two Circular Inclusions Locating on the x Axis [6]. Two inclusions with radii of r_1 and r_2 under the remote shear are considered as shown in Fig. 7(a). The stress distributions in the matrix including the radial component σ_{zr} and the tangential component $\sigma_{z\theta}$ around the circular boundary of radius r_1 are plotted in Figs. 7(b) and 7(c) for various inclusion spacings when the two inclusion radii are equal-sized ($r_1=r_2$). Two limiting cases are considered for rigid inclusions ($\mu_1/\mu_0=\mu_2/\mu_0=\infty$) and for cavities ($\mu_1/\mu_0=\mu_2/\mu_0=0.0$). It can be found that $\sigma_{z\theta}=0$ or $\sigma_{zr}=0$ for rigid inclusions or cavities as predicted for the single inclusion or cavity, respectively. Moreover, the nonzero stress components for these two cases are identical when the stress components at infinity are interchanged, i.e., the stresses around the circular boundary σ_{zr} in one case equals to $\sigma_{z\theta}$ for the other case due to the analogy of mathematical model. It can be seen from Figs. 7(b) and 7(c) that unbounded stresses apparently occur at $\theta=180$ deg under the condition of $\sigma_{zx}^{\infty}=\tau_{\infty}$ for rigid inclusions or $\sigma_{zy}^{\infty}=\tau_{\infty}$ for cavities when two inclusions approach closely or even touch each other. In Figs. 7(d) and 7(e), the variation of stresses around the circular boundary of radius r_1 is shown versus radius r_2 for a fixed separation of $d=0.1r_1$. More terms of Fourier series are required to capture the singular behavior when the two inclusions approach each other as well as the two radii of inclusions are quite different. The present numerical results match very well with those by Goree and Wilson [6].

4.4 Case 4: Two Circular Inclusions Locating on the y Axis [1]. The infinite medium with two elastic inclusions is under the uniform remote shear $\sigma_{zy}^{\infty}=\tau_{\infty}$. The first inclusion centered at the origin of radius r_1 with the shear modulus $\mu_1=2\mu_0/3$ and the other inclusion of radius $r_2=2r_1$ centered on y axis at r_1+r_2+d ($d=0.1r_1$) with the shear modulus $\mu_2=13\mu_0/7$ are shown in Fig. 8(a). In order to be compared with the Honein et al.'s data obtained by using the Möbius transformations [1], the stresses along the boundary of radius r_1 is shown in Fig. 8(b). It satisfies the equilibrium traction along the interface of circular boundary. The stress concentration factor reaches maximum at $\theta=0$ deg in the matrix. Figure 8(c) shows that only few terms of Fourier series can yield acceptable results. Figures 8(d) and 8(e) indicates that our formulation is free of boundary-layer effect since stresses σ_{zr} and $\sigma_{z\theta}$ near the boundary can be smoothly predicted, respectively. The key to eliminate the boundary-layer effect is that we introduce the degenerate kernel to describe the jump function for interior and exterior regions as shown in Table 1.

4.5 Case 5: Two Inclusions Located on the x Axis Under the Two-Direction Shear [8]. In Fig. 9(a), the parameters used in the calculation are taken as $r_1=r_2$, $\sigma_{zx}^{\infty}=\sigma_{zy}^{\infty}=\tau_{\infty}$, $\mu_0=0.185$, and $\mu_1=\mu_2=4.344$. Figure 9(b) shows stress distributions σ_{zx} and σ_{zy}

Table 3 Flowchart of the present method

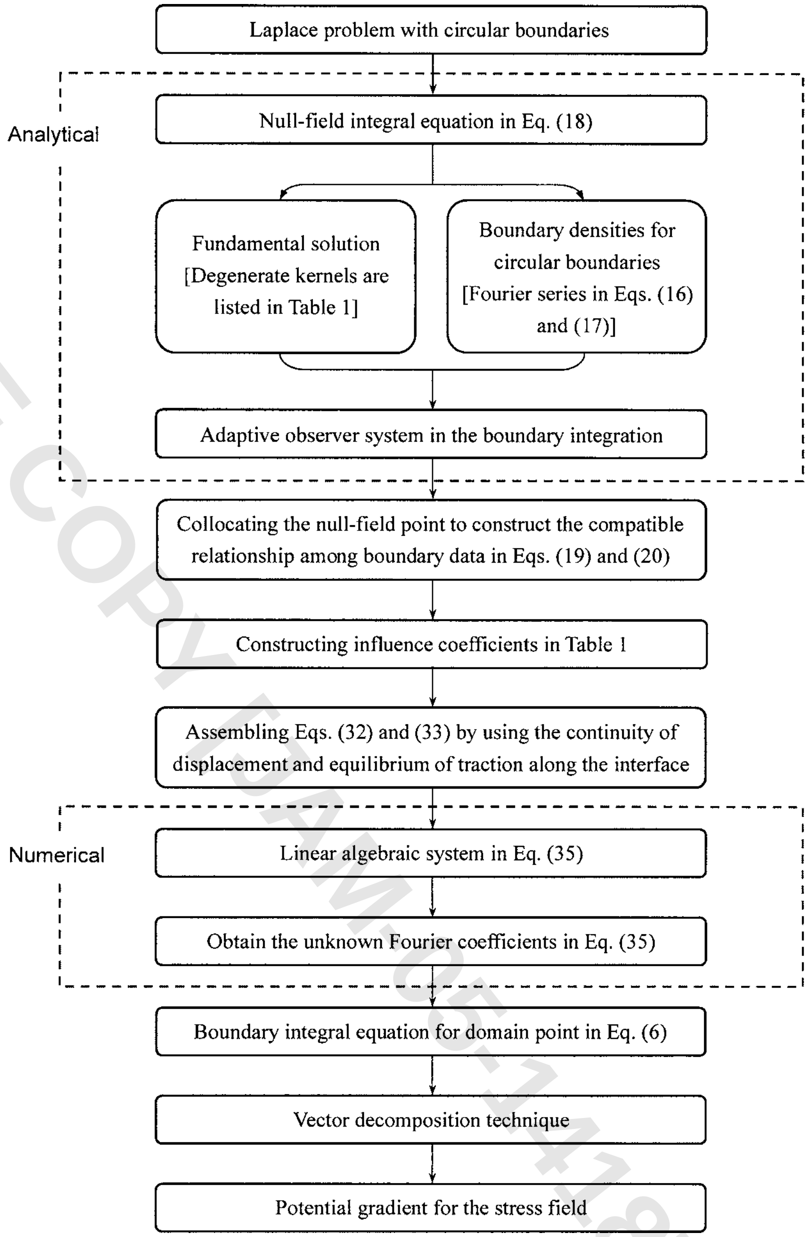

along the x axis when $d=0.1$. It can be seen that the stress component σ_{zx} is continuous across the interface between two different materials and has a peak value between two inclusions. The stress component σ_{zy} is discontinuous across the interface of two different materials. Figures 9(c) and 9(d) illustrate stress distributions of σ_{zx} and σ_{zy} along the x axis when $d=0.4$ and $d=1.0$, respectively. Both figures indicate that stress components σ_{zx} and σ_{zy} have similar changing curves to those of Fig. 9(b). However, it should be noted that the maximum value of stress component σ_{zx} drops when the distance d between the two inclusions increases. Figure 9(e) illustrates the normal stress σ_{zr} distributions along the contour $(1.001, \theta)$ for various cases of $d=0.1$, 0.5, and 1.0. It shows that the shear stress σ_{zr} increases as the distance d between the two inclusions decreases at the point where two inclusions approach each other. However, the distance d has a slight effect on σ_{zr} when the angle is in the range of 90 deg $< \theta <$ 320 deg. Figure 9(f) illustrates the tangential stress $\sigma_{z\theta}$ distributions along the contour $(1.001, \theta)$ for various distances of $d=0.1$, 0.5, and 1.0. It should be noted that the absolute value of tangential stress $\sigma_{z\theta}$ is very small in comparison with that of σ_{zr}. Figure 9(g) illustrates the variation of stress components σ_{zx} and σ_{zy} in the matrix at the point (1.001, 0 deg) versus the distance d between the two inclusions. From the figure, it can be seen that stress components σ_{zx} and σ_{zy} have higher values when the two inclusions approach each other. However, stress components σ_{zx} and σ_{zy} tend smoothly to the constant when the two inclusions separate away. Figure 9(h) shows stress distributions σ_{zx} and σ_{zy} along the x axis when the two inclusions touch each other. It can be seen that the shear stress σ_{zx} has a peak value at the touched point. For the increasing value of x, σ_{zx} tends to match the remote shear τ_∞. Besides, the stress component σ_{zy} is continuous at the tangent point $(x/r_1=1.0)$ and has a discontinuous jump on the interface between the matrix and inclusion $(x/r_1=3.0)$. The present results in Figs. 9(b)–9(h) agree very well with the Wu's data [8]. Only the stress component σ_{zx} at

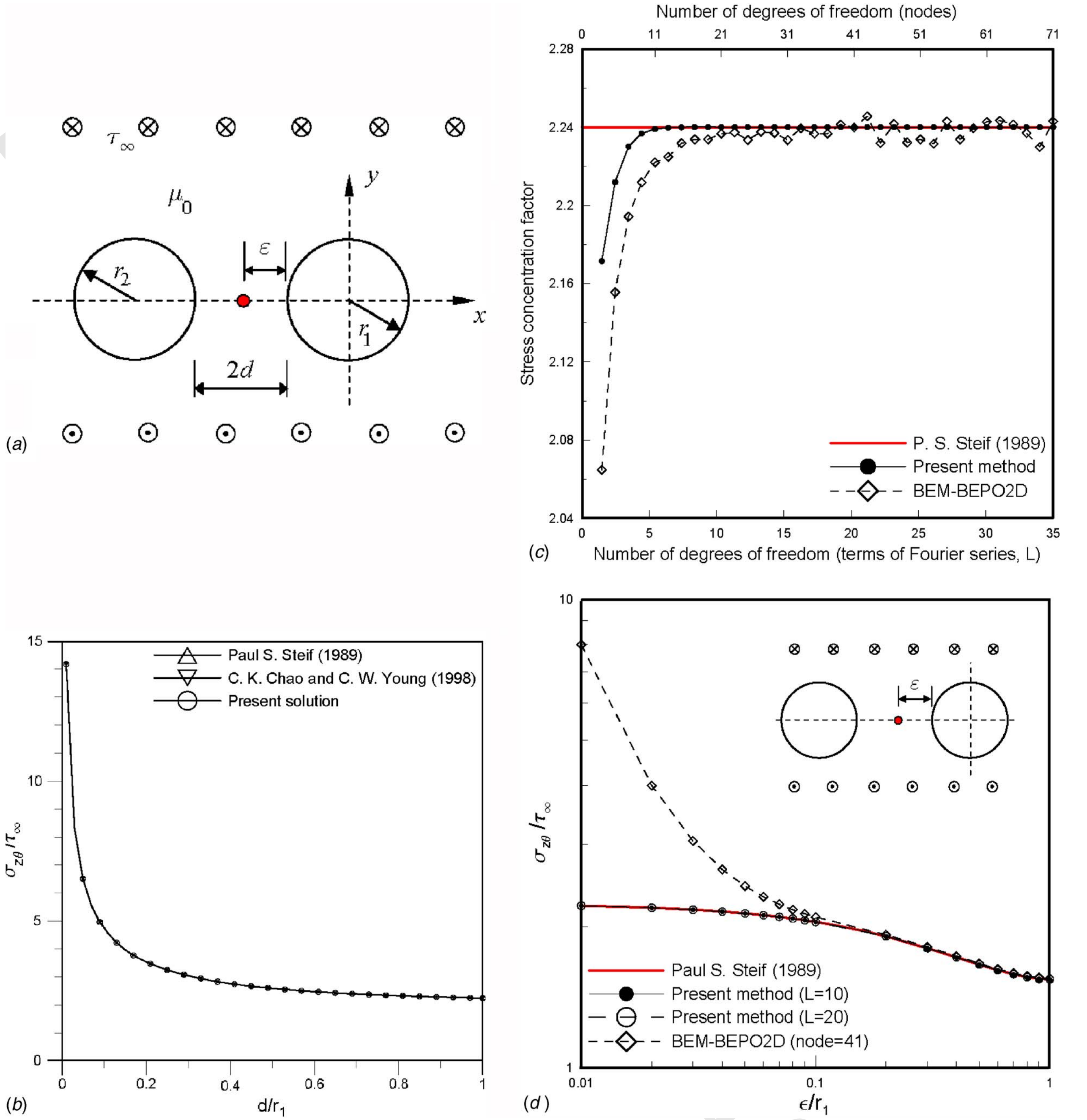

Fig. 5 (*a*) Two equal-sized holes ($r_1=r_2$) with centers on the *x* axis, (*b*) stress concentration of the problem containing two equal-sized holes, (*c*) convergence test of the problem containing two equal-sized holes ($d=1.0$), and (*d*) tangential stress in the matrix near the boundary ($d=1.0$)

the touched point is lower than the Wu's data as shown in Fig. 9(*h*), since separate Fourier expansions are described for the touched inclusions in our formulation.

4.6 Case 6: One Hole Surrounded by Two Circular Inclusions [9]. Figure 10(*a*) shows that a circular hole centered at the origin of radius r_1 is surrounded by two circular inclusions ($d/r_1=1.0$) with equal radius $r_2=r_3=2r_1$ and equal shear modulus $\mu_2=\mu_3$ under the remote shear $\sigma_{zx}^{\infty}=\tau_{\infty}$. We solved the distribution of the tangential stress along the circular hole influenced by the surrounding inclusions when they are arrayed in parallel ($\beta=0$ deg) or perpendicular ($\beta=90$ deg) to the direction of uniform shear as shown in Figs. 10(*b*) and 10(*c*). It is found that, when a hole and two inclusions are arrayed parallel to the applied load ($\beta=0$ deg), the stress concentration factor, reaching maximum at $\theta=90$ deg along a circular hole, increases (or decreases) as the neighboring hard (or soft) inclusions approach a circular hole as shown in Figs. 10(*b*) and 10(*d*). On the contrary, when a hole and two inclusions are perpendicular to the applied load ($\beta=90$ deg), the stress concentration factor, reaching maximum at $\theta=90$ deg, decreases (or increases) as the neighboring hard (or soft) inclusions approach a circular hole as shown in Figs. 10(*c*) and 10(*e*). Our numerical results match very well with the Chao and Young's results [9].

4.7 Case 7: Three Identical Inclusions Forming an Equilateral Triangle [10]. Figure 11(*a*) shows that three identical inclusions ($r_1=r_2=r_3$) subjected to the uniform shear stress σ_{zy}^{∞}

Table 4 Stress concentration factors and errors for various distances between two inclusions using the present approach and BEM

		d/r_1	0.01	0.2	0.4	0.6	0.8	1.0
Stress concentration factor	Analytical solution [2]		14.2247	3.5349	2.7667	2.4758	2.3274	2.2400
	Present method	$L=10$	10.5096 (26.12%)	3.5306 (0.12%)	2.7664 (0.01%)	2.4758 (0.00%)	2.3274 (0.00%)	2.2400 (0.00%)
		$L=20$	13.3275 (6.31%)	3.5349 (0.00%)	2.7667 (0.00%)	2.4758 (0.00%)	2.3274 (0.00%)	2.2400 (0.00%)
	BEM BEPO2D	$node=21$	7.2500 (49.03%)	3.4532 (2.31%)	2.738 (1.04%)	2.4639 (0.48%)	2.3168 (0.46%)	2.2366 (0.15%)
		$node=41$	10.2008 (28.29%)	3.5188 (0.46%)	2.7619 (0.17%)	2.4747 (0.04%)	2.3312 (0.16%)	2.2398 (0.01%)

Data in parentheses denote error.

$=\tau_\infty$ at infinity. The three inclusions form an equilateral triangle and are placed at a distance $d=4r_1$ apart. We evaluate the hoop stress $\sigma_{z\theta}$ in the matrix around the boundary of the inclusion located at the origin as shown in Fig. 11(*b*). Good agreement is obtained between the Gong's results [10] and ours. It is obvious that the limiting case of circular holes ($\mu_1/\mu_0=\mu_2/\mu_0=\mu_3/\mu_0=0.0$) leads to the maximum stress concentration at $\theta=0$ deg, which is larger than 2 of a single hole due to the interaction effect. It is also interesting to note that the stress component $\sigma_{z\theta}$ vanishes in the case of rigid inclusions ($\mu_1/\mu_0=\mu_2/\mu_0=\mu_3/\mu_0=\infty$), which can be explained by a general analogy between solutions for traction-free holes and those involving rigid inclusions [2].

5 Conclusions

A semi-analytical formulation for multiple circular inclusions with arbitrary radii, moduli, and locations using degenerate kernels and Fourier series in the adaptive observer system was developed to ensure the exponential convergence. Generally speaking, only ten terms of Fourier series ($L=10$) can obtain the acceptable and accurate results. More terms of Fourier series are required to capture the singular behavior when the two inclusions approach each other as well as the two radii of inclusions are quite different. The singularity and hypersingularity were avoided after introducing the concept of degenerate kernels for interior and exterior regions. Besides, the boundary-layer effect for the stress calculation is eliminated since the degenerate kernel can describe the jump behavior for interior and exterior domains, respectively. The exact solution for a single inclusion was also rederived by using the present formulation. Several examples investigated by Steif [2], Budiansky and Carrier [3], Goree and Wilson [6], Honein et al. [1], Wu [8], Chao and Young [9], and Gong [10] were revisited, respectively. Good agreements were made after comparing with the previous results. Regardless of the number, size, and the position of circular inclusions and cavities, the proposed method can offer good results. Moreover, our method presented here can be applied to Laplace problems with circular boundaries, e.g.,

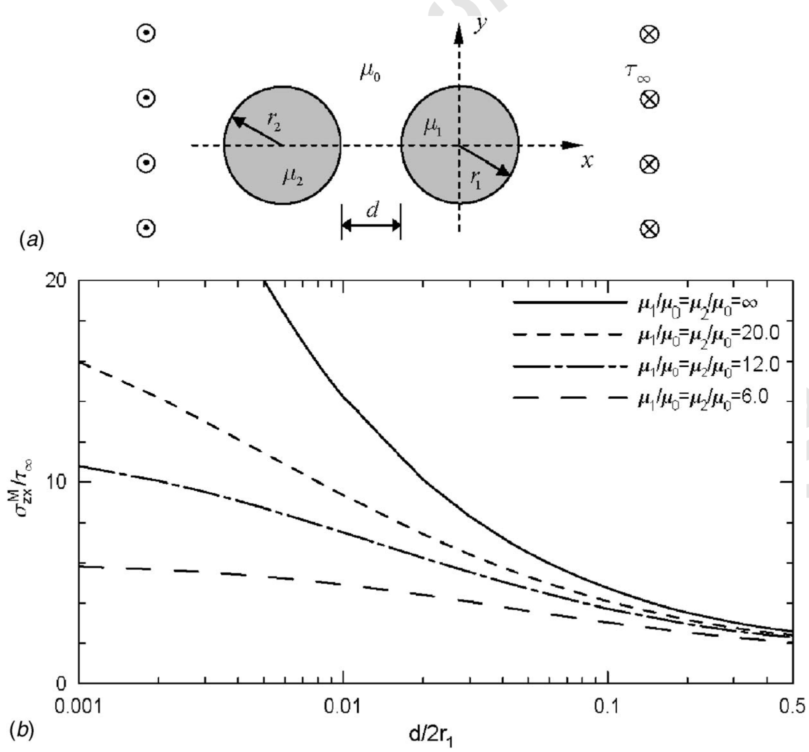

Fig. 6 (*a*) Two identical inclusions with centers on the *x* axis and (*b*) average shear stress of inclusion versus fiber spacing

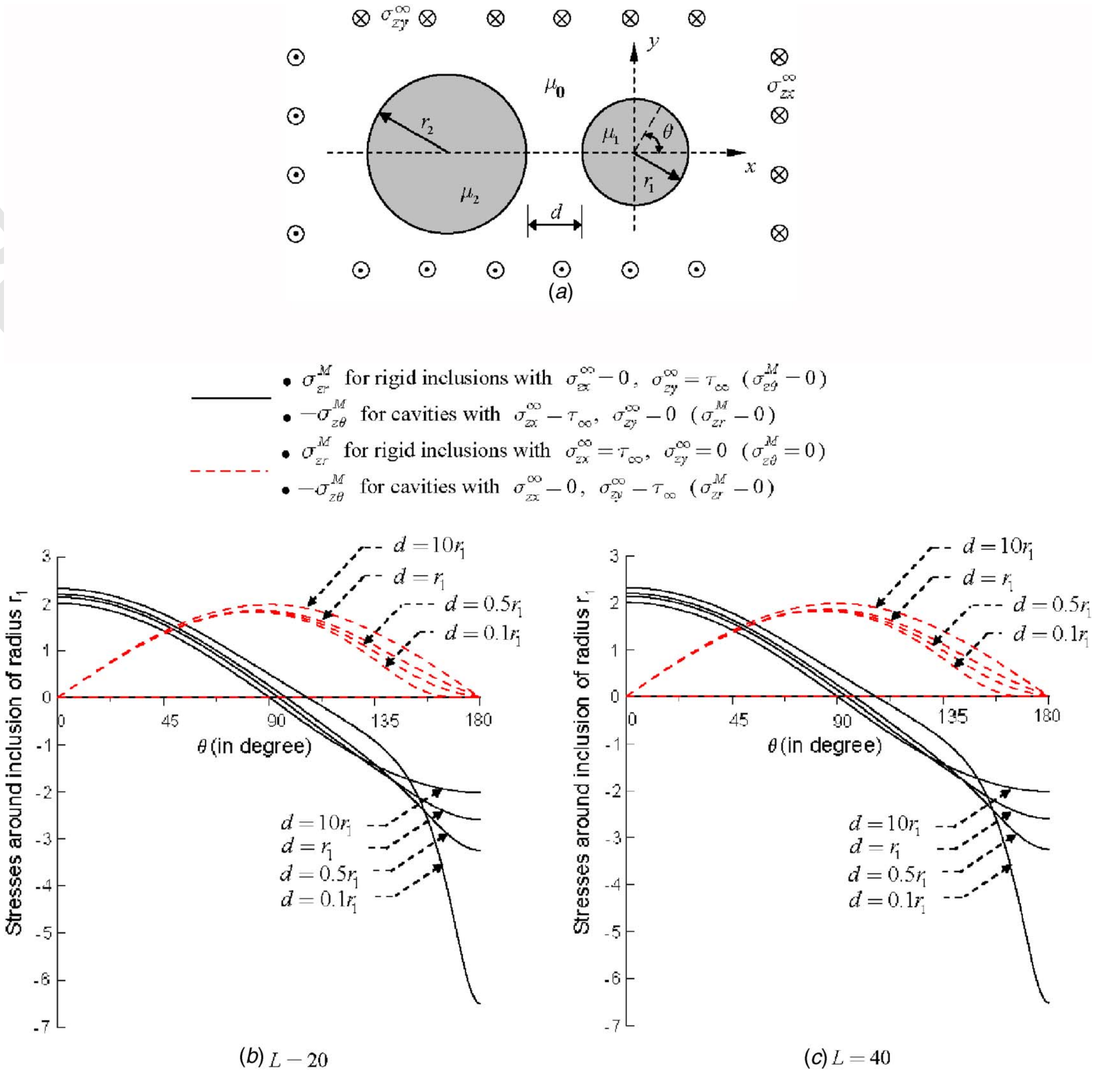

Fig. 7 (***a***) **Two circular inclusions with centers on the *x* axis, (*b*) effects of spacing on the stresses around the boundary of radius r_1 for two equal-sized inclusions (*L*=20), (*c*) effects of spacing on the stresses around the boundary of radius r_1 for two equal-sized inclusions (*L*=40), (*d*) effects of the size of neighboring inclusion on the stresses around the boundary of radius r_1 with d=0.1r_1 (*L*=80), and (*e*) effects of the size of neighboring inclusion on the stresses around the boundary of radius r_1 with d=0.1r_1 (*L*=100)**

electrostatic and magnetic problems. Besides, extensions to Helmholtz and biharmonic operators as well as 3D problems are straightforward.

Acknowledgment

The second author (A.C.W.) would like to thank Wen-Cheng Shen for valuable discussions and the student scholarship from the China Engineering Consultants, Inc., Taiwan. The present work was supported by the National Science Council of Taiwan, through Grant No. NSC94-2211-E-019-009.

Appendix A: Calculation for the Forcing Term {a}

According to Eqs. (2) and (3), the displacement and traction fields in the infinite medium due to the remote shear σ_{zx}^{∞} and σ_{zy}^{∞} in Fig. 1(d) are

$$w^{\infty}=\frac{\sigma_{zx}^{\infty}}{\mu_0}x+\frac{\sigma_{zy}^{\infty}}{\mu_0}y, \tag{A1}$$

$$t^{\infty}=\frac{\partial w^{\infty}}{\partial}=-\left(\frac{\sigma_{zx}^{\infty}}{\mu_0}n_x+\frac{\sigma_{zy}^{\infty}}{\mu_0}n_y\right), \tag{A2}$$

where the unit outward normal vector on the boundary is $n=(n_x,n_y)$. By comparing Eq. (19) with the first low of Eq. (35), we have

$$\{\mathbf{a}\}=[\mathbf{T}^M]\{\mathbf{w}^{\infty}\}-[\mathbf{U}^M]\{\mathbf{t}^{\infty}\}. \tag{A3}$$

For the circular boundary which the original system is located, the boundary condition due to the remote shear as

$$w_1^{\infty}=\frac{\sigma_{zx}^{\infty}}{\mu_0}r_1\cos\theta_1+\frac{\sigma_{zy}^{\infty}}{\mu_0}r_1\sin\theta_1, \tag{A4}$$

$$t_1^{\infty}=-\left(\frac{\sigma_{zx}^{\infty}}{\mu_0}\cos\theta_1+\frac{\sigma_{zy}^{\infty}}{\mu_0}\sin\theta_1\right). \tag{A5}$$

Considering the boundary condition, due to the remote shear, on the kth circular boundary with respect to the observer system, we have

PROOF COPY [JAM-05-1418] 008606AMJ

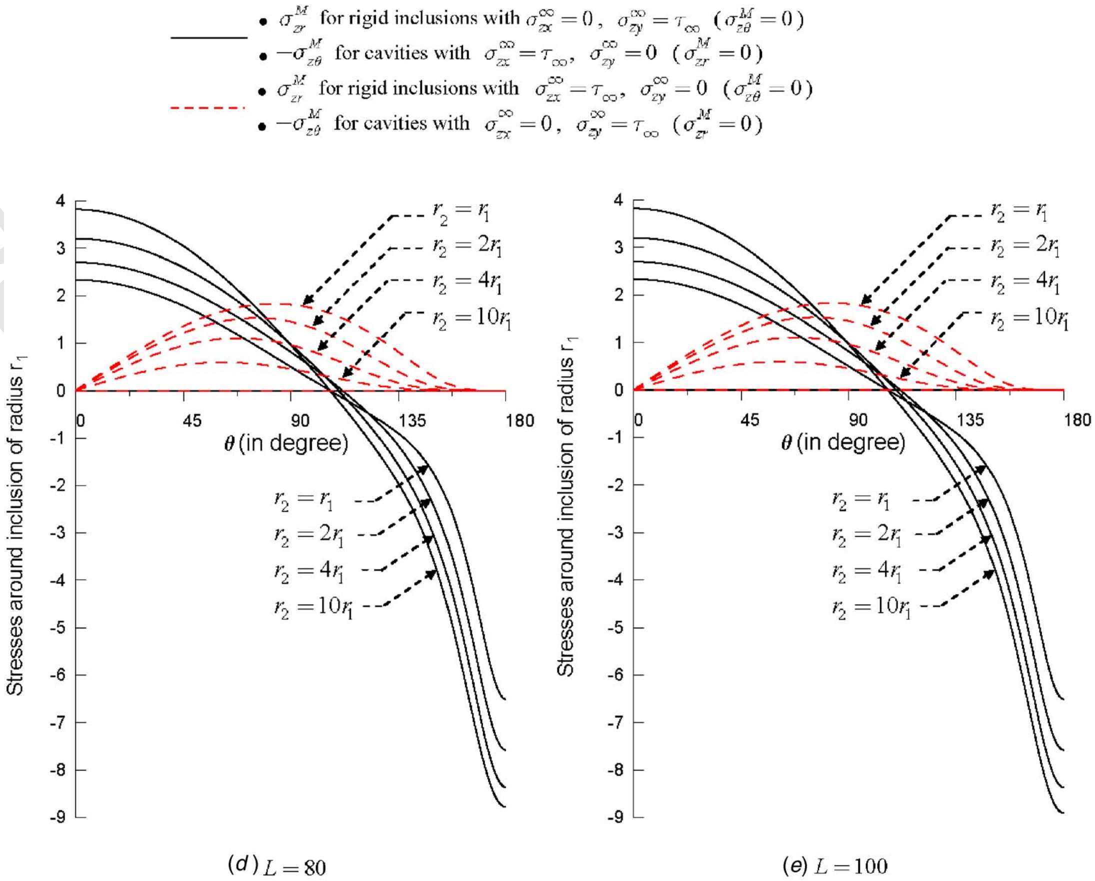

Fig. 7 (***Continued***).

$$w_k^\infty = \frac{\sigma_{zx}^\infty}{\mu_0}(e_x + r_k \cos\theta_k) + \frac{\sigma_{zy}^\infty}{\mu_0}(e_y + r_k \sin\theta_k), \qquad \text{(A6)}$$

$$t_k^\infty = -\left(\frac{\sigma_{zx}^\infty}{\mu_0}\cos\theta_k + \frac{\sigma_{zy}^\infty}{\mu_0}\sin\theta_k\right), \qquad \text{(A7)}$$

where e_x and e_y, respectively, denote the eccentric distance of kth inclusion in the x and y direction. By comparing Eq. (A5) with Eq. (A7), we find that t^∞ can be described in any observer system without any change, where θ_k denotes the polar angle in the adaptive observer coordinate system.

Appendix B: Derivation of the Exact Solution for a Single Inclusion

We derive the exact solution for antiplane problem with a single inclusion under the remote shear using the present formulation. The infinite medium under the shear stress $\sigma_{zx}^\infty = 0$ and $\sigma_{zy}^\infty = \tau_\infty$ at infinity is considered. The Fourier coefficients in Eq. (24) can be written as

$$\{\mathbf{w}^\infty\} = \begin{Bmatrix} 0 \\ 0 \\ \dfrac{\tau_\infty r_1}{\mu_0} \\ \vdots \\ 0 \\ 0 \end{Bmatrix}_{(2L+1)\times 1}, \quad \{\mathbf{t}^\infty\} = \begin{Bmatrix} 0 \\ 0 \\ -\dfrac{\tau_\infty}{\mu_0} \\ \vdots \\ 0 \\ 0 \end{Bmatrix}_{(2L+1)\times 1}, \qquad \text{(B1)}$$

where r_1 is the radius of the single inclusion. By substituting the appropriate degenerate kernels in Eqs. (12) and (13) into Eqs. (19) and (20) and employing the continuity of displacement and equilibrium of traction along the interface in Eqs. (32) and (33), the unknown boundary data in Eqs. (23) and (25) can be obtained using the symbolic software MATHEMATICA as shown below

$$\{\mathbf{w}^M\} = \begin{Bmatrix} 0 \\ 0 \\ \dfrac{2\tau_\infty r_1}{\mu_0 + \mu_1} \\ \vdots \\ 0 \\ 0 \end{Bmatrix}_{(2L+1)\times 1}, \quad \{\mathbf{t}^M\} = \begin{Bmatrix} 0 \\ 0 \\ \dfrac{-2\tau_\infty \mu_1}{\mu_0(\mu_0 + \mu_1)} \\ \vdots \\ 0 \\ 0 \end{Bmatrix}_{(2L+1)\times 1}, \qquad \text{(B2)}$$

$$\{\mathbf{w}^I\} = \begin{Bmatrix} 0 \\ 0 \\ \dfrac{2\tau_\infty r_1}{\mu_0 + \mu_1} \\ \vdots \\ 0 \\ 0 \end{Bmatrix}_{(2L+1)\times 1}, \quad \{\mathbf{t}^I\} = \begin{Bmatrix} 0 \\ 0 \\ \dfrac{2\tau_\infty}{\mu_0 + \mu_1} \\ \vdots \\ 0 \\ 0 \end{Bmatrix}_{(2L+1)\times 1}. \qquad \text{(B3)}$$

After substituting Eqs. (B1) and (B2) into the boundary integral equation for the domain point in Eq. (6), we obtain the total stress fields in the matrix

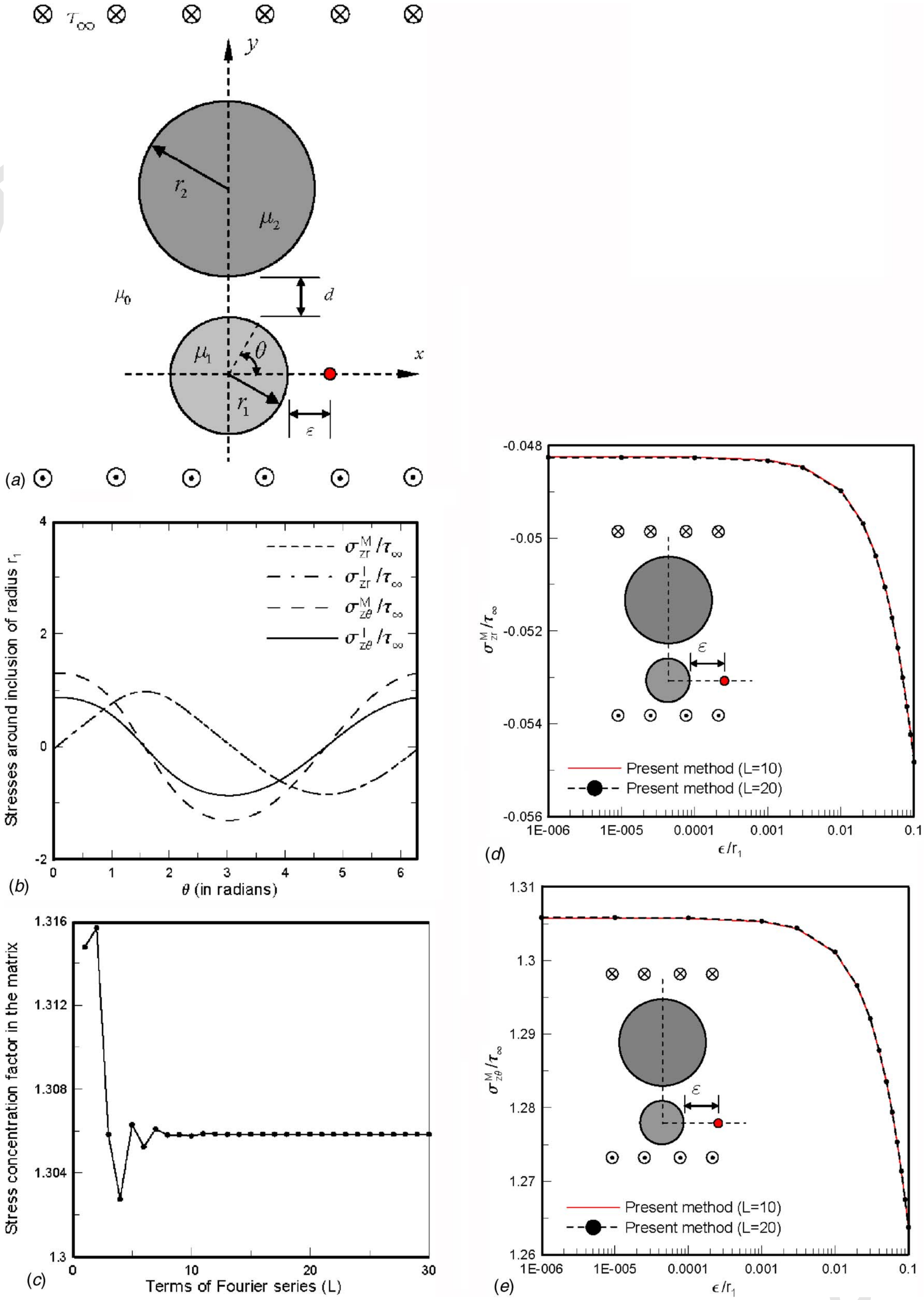

Fig. 8 (***a***) **Two circular inclusions with centers on the** ***y*** **axis, (*b*) stresses around the circular boundary of radius r_1, (*c*) convergence test of the two-inclusions problem, (*d*) radial stress in the matrix near the boundary, and (*e*) tangential stress in the matrix near the boundary**

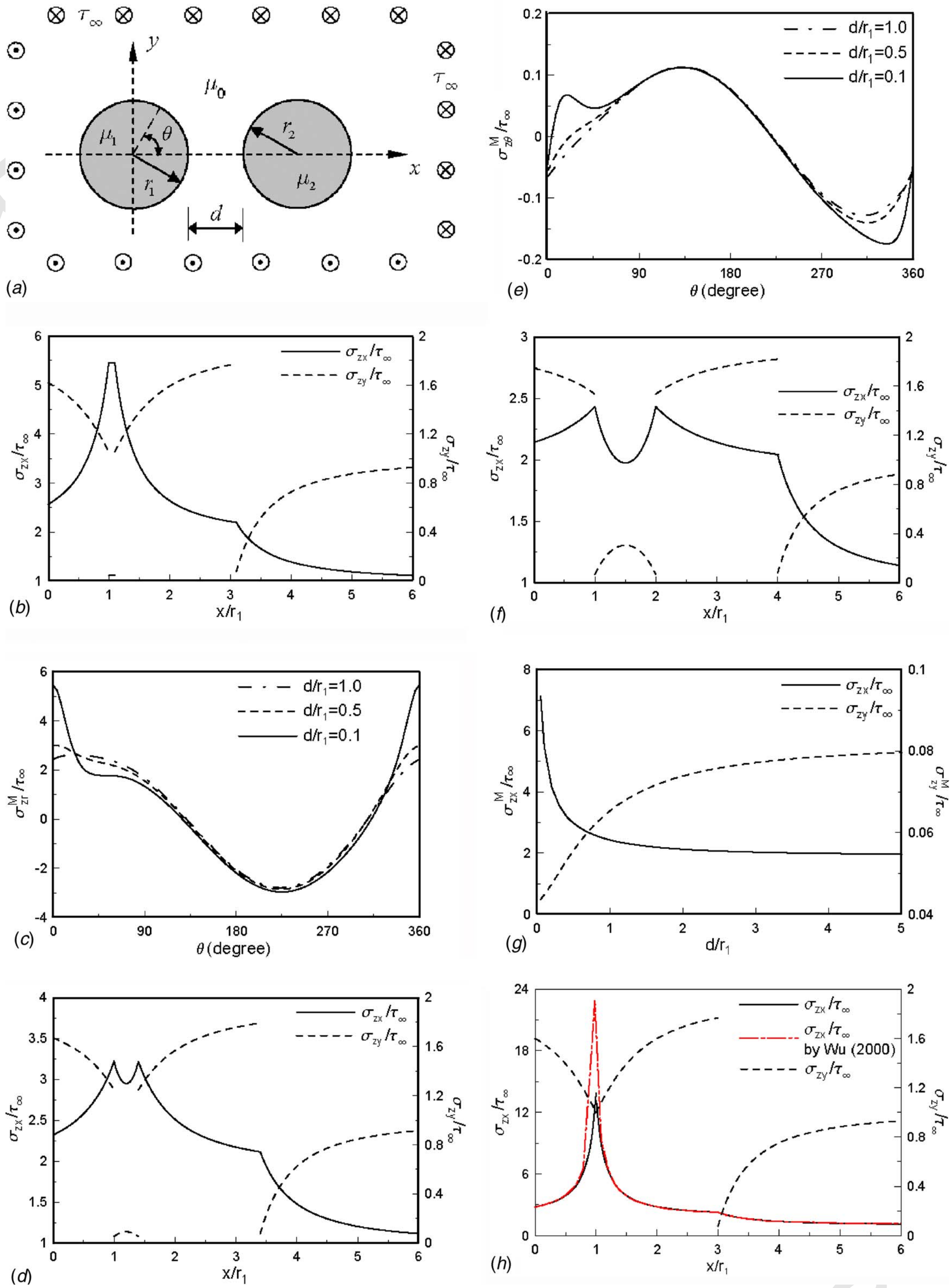

Fig. 9 (*a*) Two circular inclusions embedded in a matrix under the remote antiplane shear in two directions, (*b*) stress distributions along the *x* axis when $d=0.1$, (*c*) stress distributions along the *x* axis when $d=0.4$, (*d*) stress distributions along the *x* axis when $d=1.0$, (*e*) normal stress distributions along the contour $(1.001,\theta)$, (*f*) tangential stress distributions along the contour $(1.001,\theta)$, (*g*) variations of stresses at the point (1.001, 0 deg), and (*h*) stress distributions along the *x* axis when the two inclusions touch each other

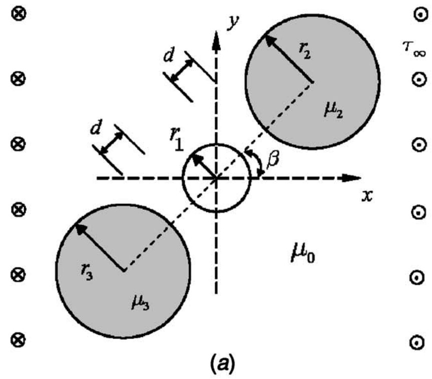

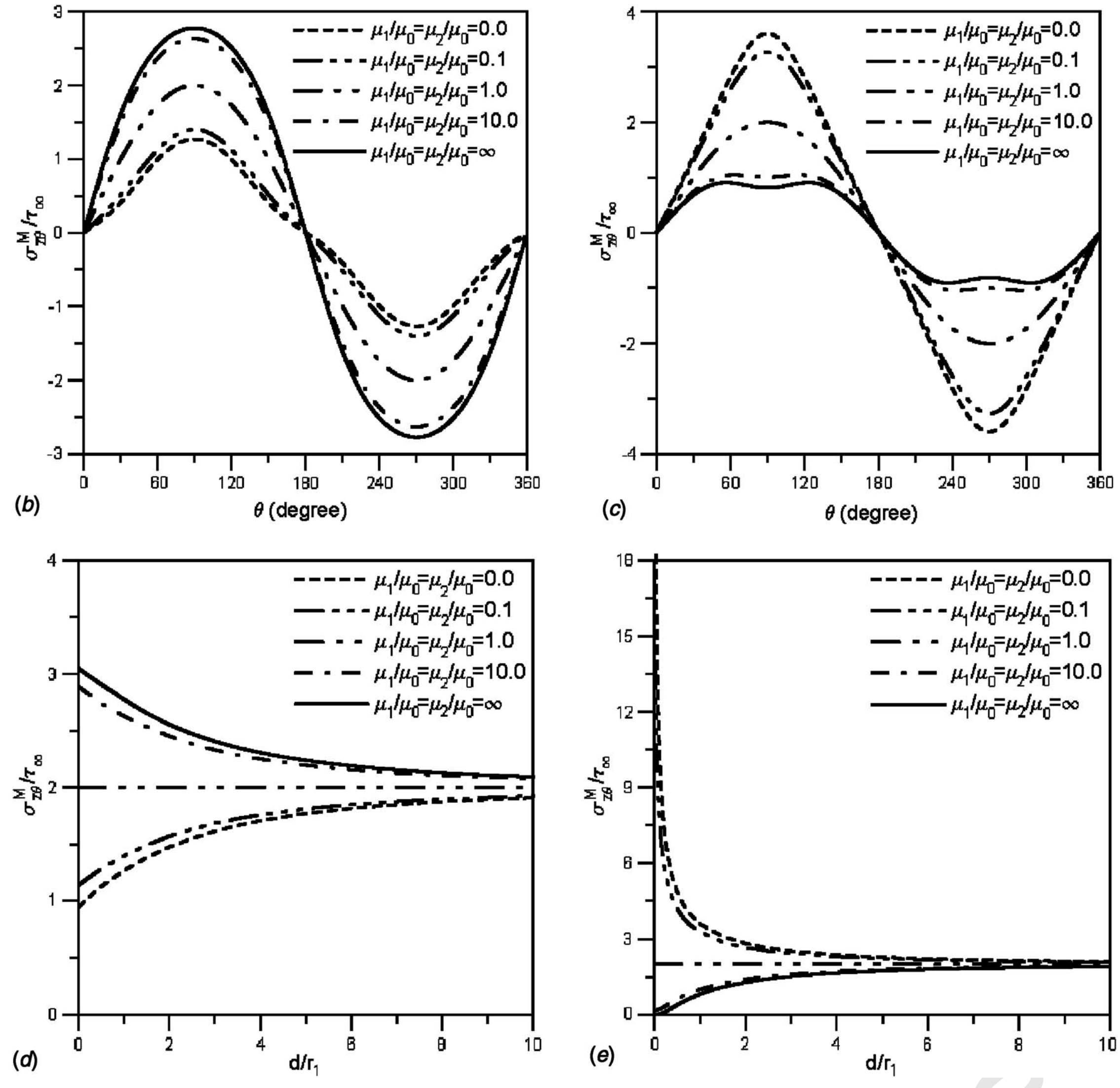

Fig. 10 (*a*) One hole surrounded by two circular inclusions, (*b*) tangential stress distribution along the hole boundary with $\beta=0$ deg, (*c*) tangential stress distribution along the hole boundary with $\beta=90$ deg, (*d*) stress concentration as a function of the spacing d/r_1 with $\beta=0$ deg, and (*e*) stress concentration as a function of the spacing d/r_1 with $\beta=90$ deg

PROOF COPY [JAM-05-1418] 008606AMJ

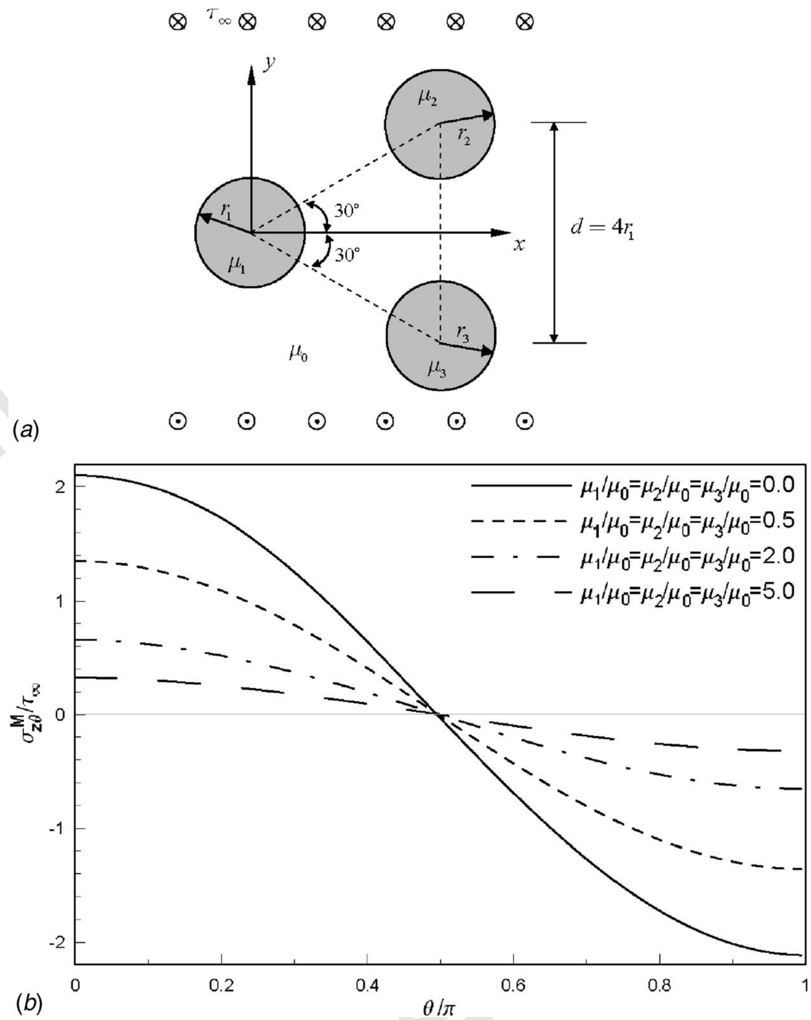

Fig. 11 (*a*) **Three identical inclusions forming an equilateral triangle, and** (*b*) **tangential stress distribution around the inclusion located at the origin**

$$\sigma_{zx}^M = \mu_0 \frac{\partial w^M}{\partial x} + \sigma_{zx}^\infty = -2\tau_\infty \frac{r_1^2}{\rho^2} \frac{\mu_0 - \mu_1}{\mu_0 + \mu_1} \sin\phi \cos\phi,$$

$$r_1 \leqslant \rho \leqslant \infty, \quad 0 \leqslant \phi \leqslant 2\pi, \tag{B4}$$

$$\sigma_{zy}^M = \mu_0 \frac{\partial w^M}{\partial y} + \sigma_{zy}^\infty = \tau_\infty \frac{r_1^2}{\rho^2} \frac{\mu_0 - \mu_1}{\mu_0 + \mu_1} (\cos^2\phi - \sin^2\phi) + \tau_\infty,$$

$$r_1 \leqslant \rho \leqslant \infty, \quad 0 \leqslant \phi \leqslant 2\pi. \tag{B5}$$

After substituting Eq. (B3) into the boundary integral equation for the domain point in Eq. (6), we have the total stress fields in the inclusion

$$\sigma_{zx}^I = \mu_1 \frac{\partial w^I}{\partial x} = 0, \quad 0 \leqslant \rho \leqslant r_1, \quad 0 \leqslant \phi \leqslant 2\pi, \tag{B6}$$

$$\sigma_{zy}^I = \mu_1 \frac{\partial w^I}{\partial y} = 2\tau_\infty \frac{\mu_1}{\mu_0 + \mu_1}, \quad 0 \leqslant \rho \leqslant r_1, \quad 0 \leqslant \phi \leqslant 2\pi. \tag{B7}$$

Finally, the stress components σ_{zr} and $\sigma_{z\theta}$ in Eqs. (38) and (39) can be superimposed by using σ_{zx} and σ_{zy} as shown below

$$\sigma_{zr}^M = 2\tau_\infty \frac{r_1^2}{\rho^2} \frac{\mu_1}{\mu_0 + \mu_1} \sin\phi, \quad r_1 \leqslant \rho \leqslant \infty, \quad 0 \leqslant \phi \leqslant 2\pi, \tag{B8}$$

$$\sigma_{z\theta}^M = 2\tau_\infty \frac{r_1^2}{\rho^2} \frac{\mu_0}{\mu_0 + \mu_1} \cos\phi, \quad r_1 \leqslant \rho \leqslant \infty, \quad 0 \leqslant \phi \leqslant 2\pi, \tag{B9}$$

$$\sigma_{zr}^I = 2\tau_\infty \frac{\mu_1}{\mu_0 + \mu_1} \sin\phi, \quad 0 \leqslant \rho \leqslant r_1, \quad 0 \leqslant \phi \leqslant 2\pi, \tag{B10}$$

$$\sigma_{z\theta}^I = 2\tau_\infty \frac{\mu_1}{\mu_0 + \mu_1} \cos\phi, \quad 0 \leqslant \rho \leqslant r_1, \quad 0 \leqslant \phi \leqslant 2\pi. \tag{B11}$$

It is obvious to see that the maximum stress concentration occurs at $\rho = r_1$ and $\phi = 0$. It is noted that σ_{zr}^M coincides with σ_{zr}^I as required by the traction equilibrium on the interface between the matrix and inclusion. It is found that the stress concentration factor is reduced due to the inclusion in comparison with that of cavity ($\mu_1 = 0$) as shown in Eq. (B8). The exact solution for a single inclusion using the present formulation matches well with the previous one obtained by employing the complex-variable formulation [1].

References

[1] Honein, E., Honein, T., and Herrmann, G., 1992, "On Two Circular Inclusions in Harmonic Problems," Q. Appl. Math., **50**, pp. 479–499.

[2] Steif, P. S., 1989, "Shear Stress Concentration Between Holes," ASME J. Appl. Mech., **56**, pp. 719–721.

[3] Budiansky, B., and Carrier, G. F., 1984, "High Shear Stresses in Stiff-Fiber Composites," ASME J. Appl. Mech., **51**, pp. 733–735.

[4] Zimmerman, R. W., 1988, "Second-Order Approximation for the Compression of an Elastic Plate Containing a Pair of Circular Holes," Z. Angew. Math. Mech., **68**, pp. 575–577.

[5] Sendeckyj, G. P., 1971, "Multiple Circular Inclusion Problems in Longitudinal Shear Deformation," J. Elast., **1**(1), pp. 83–86.

[6] Goree, J. G., and Wilson, H. B., 1967, "Transverse Shear Loading in an Elastic Matrix Containing Two Circular Cylindrical Inclusions," ASME J. Appl. Mech., **34**, pp. 511–513.

[7] Bird, M. D., and Steele, C. R., 1992, "A Solution Procedure for Laplace's Equation on Multiply-Connected Circular Domains," ASME J. Appl. Mech., **59**, pp. 398–404.

[8] Wu, L. Z., 2000, "Interaction of Two Circular Cylindrical Inhomogeneities Under Anti-Plane Shear," Compos. Sci. Technol., **60**, pp. 2609–2615.

[9] Chao, C. K., and Young, C. W., 1998, "On the General Treatment of Multiple Inclusions In Antiplane Elastostatics," Int. J. Solids Struct., **35**, pp. 3573–3593.

[10] Gong, S. X., 1995, "Antiplane Interaction Among Multiple Circular Inclusions," Mech. Res. Commun., **22**(3), pp. 257–262.

[11] Chou, S. I., 1997, "Stress Field Around Holes in Antiplane Shear Using Complex Variable Boundary Element Method," ASME J. Appl. Mech., **64**, pp. 432–435.

[12] Ang, W. T., and Kang, I., 2000, "A Complex Variable Boundary Element Method for Elliptic Partial Differential Equations in a Multiple-Connected Region," Int. J. Comput. Math., **75**, pp. 515–525.

[13] Mogilevskaya, S. G., and Crouch, S. L., 2001, "A Galerkin Boundary Integral Method for Multiple Circular Elastic Inclusions," Int. J. Numer. Methods Eng., **52**, pp. 1069–1106.

[14] Kress, R., 1989, *Linear Integral Equations*, Springer-Verlag, Berlin.

[15] Chen, J. T., Kuo, S. R., and Chen, K. H., 1999, "A Nonsingular Integral Formulation for the Helmholtz Eigenproblems of a Circular Domain," J. Chin. Inst. Eng., **22**(6), pp. 729–739.

[16] Chen, J. T., and Kuo, S. R., 2000, "On Fictitious Frequencies Using Circulants for Radiation Problems of a Cylinder," Mech. Res. Commun., **27**(1), pp. 49–58.

[17] Chen, J. T., Kuo, S. R., and Lin, J. H., 2002, "Analytical Study and Numerical Experiments for Degenerate Scale Problems in the Boundary Element Method for Two-Dimensional Elasticity," Int. J. Numer. Methods Eng., **54**(12), pp. 1669–1681.

[18] Chen, J. T., Shen, W. C., and Wu, A. C., 2006, "Null-Field Integral Equations for Stress Field Around Circular Holes Under Antiplane Shear," Eng. Anal. Boundary Elem., **30**, pp. 205–217.

[19] Chen, J. T., Hsiao, C. C., and Leu, S. Y., 2006, "Null-Field Integral Equation Approach for Plate Problems With Circular Boundaries," ASME J. Appl. Mech., to be published.

[20] Chen, J. T., and Hong, H.-K., 1999, "Review of Dual Boundary Element Methods With Emphasis on Hypersingular Integrals and Divergent Series," Appl. Mech. Rev., **52**, pp. 17–33.

[21] Chen, J. T., and Chiu, Y. P., 2002, "On the Pseudo-Differential Operators in the Dual Boundary Integral Equations Using Degenerate Kernels and Circulants," Eng. Anal. Boundary Elem., **26**, pp. 41–53.

[22] Lebedev, N. N., Skalskaya, I. P., and Uyand, Y. S., 1979, *Worked Problem in Applied Mathmatics*, Dover, New York.